Optics and Lasers in Engineering 149 (2022) 106793

Contents lists available at ScienceDirect

Optics and Lasers in Engineering

journal homepage: www.elsevier.com/locate/optlaseng

Calibration and rectification of bi-telecentric lenses in Scheimpflug condition

Yan Hu [a,b,c], Zhongwei Liang [a,b,c], Shijie Feng [a,b,c], Wei Yin [a,b,c], Jiaming Qian [a,b,c], Qian Chen [a,b,*], Chao Zuo [a,b,c,*]

[a] School of Electronic and Optical Engineering, Nanjing University of Science and Technology, No. 200 Xiaolingwei Street, Nanjing, Jiangsu Province 210094, China
[b] Jiangsu Key Laboratory of Spectral Imaging & Intelligent Sense, Nanjing, Jiangsu Province 210094, China
[c] Smart Computational Imaging Laboratory (SCILab), Nanjing University of Science and Technology, Nanjing, Jiangsu Province 210094, China

ARTICLE INFO

Keywords:
Scheimpflug
Telecentric
Stereo-rectification
Optical metrology
Microscopy

ABSTRACT

In the lens-based imaging model, the Scheimpflug principle is expressed as the object plane, the image plane, and the lens plane intersect in a line. With this principle, the focused object plane in the lens's object side can be tilted by placing a tilted sensor at the image side of the lens; thereby, multi-cameras can be focused on the same object space with an overlapping field of view and depth of field. For Scheimpflug cameras, additional tilt angles between the camera sensor and the optical axis are introduced, which has been well studied in pinhole cameras' calibration methods. Telecentric lens, as a commonly used lens type, has constant magnification in the axial direction and has a wide range of applications in close-range photogrammetry. To calibrate and rectify the telecentric lenses in Scheimpflug conditions, we derived a concise imaging model by expressing the sensor tilt angles and the lens magnification into a simplified intrinsic matrix. Based on the derived imaging model, an integrated calibration algorithm without solving the tilt angles and a stereo-rectification method for stereo matching are developed. The effectiveness and accuracy of the proposed methods are verified by experiments, including the comparison with the traditional telecentric model and pinhole model. Combined with the experimental results, we analyzed the potential impact of the extrinsic rotation matrix's ambiguity, verified whether the lens distortion affects the re-projection error, and discussed how the calibration posture influences the calibration accuracy.

1. Introduction

Stereo vision plays an essential role in non-contact 3D measurement [1,2], which employs two cameras to achieve applications such as visual synthesis, terrain surveying, and deformation detection [3–7]. In the 3D measurement of small objects that require higher accuracy, the lens's working distance needs to be reduced to achieve a small field of view and a high numerical aperture. The stereo microscope is a commonly used observation tool for microscopic targets, containing two independent microscopic optical paths. Nevertheless, it is more suitable for direct observation by the human eyes and needs some modifications before it can be used for quantitative 3D measurement [8–10].

When used in machine vision applications, a telecentric lens provides an optical path with a small field of view and provides a fixed size, higher resolution, and lower distortion imaging within a considerable depth of field. These characteristics are of great significance to binocular systems under the microscopic field of view. Scholars have carried out a series of calibration methods for telecentric lenses to improve the systems' accuracy, flexibility, and efficiency involving telecentric lenses [7,11–15]. Liu et al. [16] used a 3D gauge as the calibration target and uses the factorization method and beam adjustment to realize the telecentric microscopic 3D measurement system's calibration. Although the 3D gauge can directly provide spatial data to solve all the rotation matrix parameters, it requires much higher manufacturing accuracy. For a microscopic view with a limited depth of field, the whole body of the 3D calibration block is difficult to be imaged entirely in focus.

In recent years, the plane calibration method has been proposed and developed [7,11,14,16–21]. In the perspective model camera, all parameters can be solved using only standard plane gauge [22]. Li et al. [11] proposed a telecentric lens calibration method and used it in a telecentric microscopic 3D measurement. A plane with a 2D comb function distributed circles is applied as the calibration target in this method. A neglected issue is that the depth insensitivity of a telecentric lens in the optical axis direction leads to uncertainty of the plane posture, which

* Corresponding authors at: School of Electronic and Optical Engineering, Nanjing University of Science and Technology, No. 200 Xiaolingwei Street, Nanjing, Jiangsu Province 210094, China.
E-mail addresses: chenqian@njust.edu.cn (Q. Chen), zuochao@njust.edu.cn (C. Zuo).

https://doi.org/10.1016/j.optlaseng.2021.106793
Received 18 March 2021; Received in revised form 28 June 2021; Accepted 30 August 2021
Available online 11 September 2021
0143-8166/

makes the extrinsic matrix of the imaging model challenging to determine [23,24]. To solve this problem, Chen et al. [7] proposed obtaining the image of the calibration target in a shifted position by a translation stage to help determine the normal direction of each calibration pose. Li et al. [19] proposed a microscopic fringe projection profilometry system that includes a long-distance lens for the projector and a telecentric lens for the camera. The pixel coordinates of the feature points of the projector's light path are obtained by the phase-shifting method. Then the relative position of all the calibration poses can be obtained, thereby providing the 3D coordinates of all the feature points of all calibration poses, which also solves the extrinsic ambiguity problem.

The calibration methods of telecentric cameras have been greatly improved thanks to the continuously proposed calibration algorithms. However, a problem has to be faced when conducting measurement within a small field of view, which is the depth of field is much smaller than that under the macro field of view, and the telecentric camera is no exception.

Scheimpflug principle can be described as tilting the camera sensor so that the focused object plane in front of the lens can be tilted, thereby extending the depth of field in the object space [25–30]. This is why the Scheimpflug camera offers a wide range of applications in the field of typical close-range photogrammetry, particle image velocity, and digital image correlation.

Scheimpflug principle is also used in microscopic 3D measurement with telecentric lenses. In the multi-view-based microscopic 3D measurement, there is still a problem that it is hard to make a maximized superposition of the sharply imaged area of different optical paths due to the limited depth of field [31]. Steger [32] proposed a comprehensive and versatile camera model for cameras in Scheimpflug conditions but did not provide a calculation method to get initial values of the parameters. Wang [31] applied four telecentric lenses in Scheimpflug conditions to construct a multi-view fringe projection 3D microscopy system. In this work, the cameras are calibrated using the general imaging model [33], which considers that imaging is the process of collecting incoming rays from the scene onto the sensor. Mei [30] adopted the Scheimpflug condition in a telecentric lens-based stereoscopic vision 3D measurement system. In this work, the Scheimpflug condition is calibrated using HALCON's method, which independently involves and calculates the rotation and tilt angles without considering the affine ambiguity. Peng [15] also applied the Scheimpflug telecentric lens in a fringe projection system and derived a model to compensate for the image distortion caused by the sensor tilt based on the geometric theory. However, this model is only applicable for the object side telecentric lenses and limited within a relatively small tilt angle as the tilt is molded as part of the distortion. Moreover, the model illustrated here requires that the length of the lens should be provided in advance, which in practice is not easy to obtain [28].

In this paper, in order to improve the imaging quality in multi-view 3D sensing by conveniently using the Scheimpflug condition, we propose a simplified matrix-based imaging model for a bi-telecentric lens in Scheimpflug condition by establishing a direct mapping relationship between the 3D coordinate of the object and the 2D coordinates on the camera sensor. In our method, the tilt angles of the sensor are also introduced but are converted into the magnification variation in two directions and a tangential parameter. The detailed solution of the imaging model is derived, based on which a telecentric stereo-rectification method in Scheimpflug condition is developed. In the experiments, single-camera calibration and stereo rectification of dual-Scheimpflug telecentric cameras are successfully performed, based on which we can conclude that the proposed concise imaging model is correct and the corresponding parameter solving method is effective. After homography-transform-based epipolar rectification, stereo matching processes in DIC [34] or fringe projection-based 3D measurement [35–37] are simplified into one-dimensional searching, which dramatically improves the measurement efficiency.

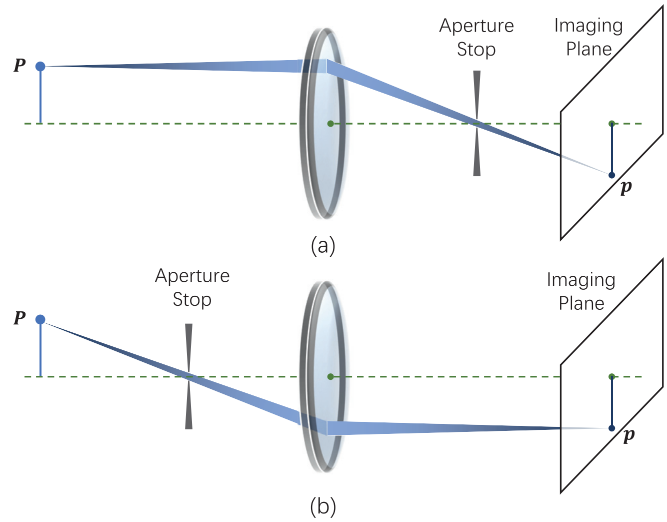

Fig. 1. The optical model of (a) an object-side telecentric lens; (b) an image-side telecentric lens. In an object-side telecentric lens, the aperture stop is installed at the focal plane in the image space; In an image-side telecentric lens, the aperture stop is installed at the focal plane in the object space.

2. The imaging model of telecentric lenses

In this section, we briefly introduce the three kinds of telecentric lenses: the object-side telecentric lenses, image-side telecentric lenses, and bi-telecentric lens (also known as the bilateral telecentric lens) in Scheimpflug condition.

2.1. Object-side and image-side telecentric lenses

The object-side telecentric lens model can be simplified to a lens with its entrance pupil is at infinity. As shown in Fig. 1(a), an aperture is added at its rear focal plane to limit the angle of the imaging light. The light emitted from point P is imaged at point p by the beam passing through this aperture only. This imaging model possesses a fixed distance between the lens and the camera sensor so that the chief ray can remain unchanged while the object point moves nearer or further along the optical axis; that is how the characteristic of constant magnification being ensured. Objects beyond the depth of field will cause the image to blur but will not change the image size. However, the imaging side has perspective characteristics. If the camera sensor moves or tilted, the imaging magnification will change or no longer maintain uniform distribution.

Some object-side telecentric lenses provide a manual focus function to facilitate the measurement of objects at different distances. However, the lens's telecentricity will lose when the object distance is too long because the very first lens will gradually replace the aperture stop as the aperture of the entire imaging system.

As the name suggests, the image-side telecentric lens has opposite characteristics to the object-side telecentric lens. Its exit pupil is located at infinity by adding an aperture stop at the focal plane in the object space shown in Fig. 1(b). An exit pupil at infinity makes the lens image-side telecentric. This property minimizes any angle-of-incidence dependence of the sensor or any beam-splitter prism assembly behind the lens, such as a color separation prism in a three-CCD camera. The uniformity of the illumination light on the image side also makes them suitable for photography and radiometry.

2.2. Bi-telecentric lens in Scheimpflug condition

As Fig. 2 shows, a bi-telecentric lens (also known as a bi-lateral telecentric lens) is composed of two sets of lenses called object-side lens

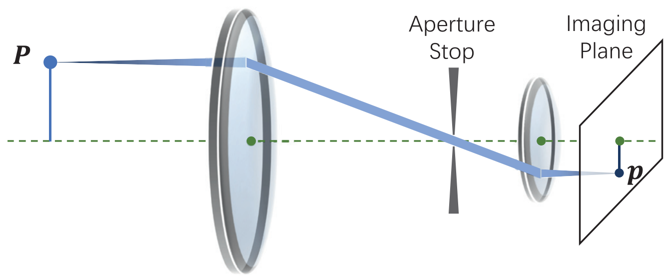

Fig. 2. The optical model of a bi-telecentric lens. The object-side lens's rear focal plane coincides with the front focal plane of the image-side lens at a common plane where an aperture stop is placed.

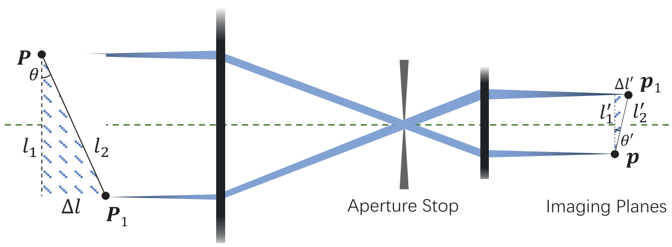

Fig. 3. The schematic of the image property of a bi-telecentric lens in Scheimpflug condition.

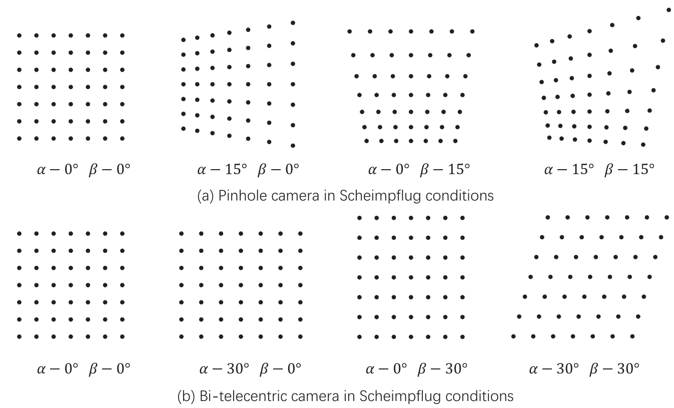

Fig. 4. The distorted images captured by a pinhole camera in Scheimpflug conditions with different tilted angles (a) and a bi-telecentric camera in Scheimpflug conditions with different tilted angles (b).

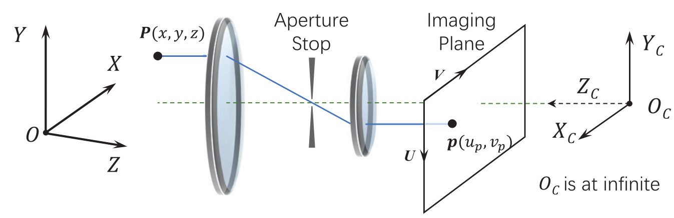

Fig. 5. Simplified schematic of the imaging process and the coordinate systems of a bi-telecentric camera.

and image-side lens, respectively. The object-side lens's rear focal plane coincides with the front focal plane of the image-side lens at a common plane where an aperture stop is placed. This aperture stop cooperates with the object-side lens to form telecentricity in the object space and cooperates with the imaging lens to form telecentricity in the image space. The magnification of the bi-telecentric lens is determined by the focal lengths of the two sets of lenses together, so no matter the working distance or the camera sensor's position changes, it will not change the optical magnification. This feature makes the bi-telecentric lens most suitable for the measurement field based on optical image processing. However, a specific working distance should be satisfied when applying bi-telecentric lenses to minimize imaging distortion and maintain perfect telecentricity.

The Scheimpflug condition can be applied in telecentric lenses to simultaneously achieve fixed magnification and considerable field imaging depth [15,30–32]. According to the Scheimpflug principle, if the angle between the camera sensor and the optical axis is changed, the camera sensor is no longer perpendicular to the optical axis. Correspondingly, the object plane conjugate to the camera sensor will also be no longer perpendicular to the optical axis.

As shown in Fig. 3 is a bi-telecentric lens imaging model in Scheimpflug condition. l_1 and $l_1^{'}$ are two lines perpendicular to the optical axis and are conjugate to each other in the object space and image space. P is an object point on l_1 in the object space, and p is the image point on $l_1^{'}$ in the image space. l_2 and $l_2^{'}$ are conjugated tilted lines in the object and image space, respectively. Point P_1 on l_2 is closer to the lens than point P and has its image point p_1 further to the lens than point p in the image space. When the distance between the object point and the lens changes, the image point is only displaced in the axial direction.

However, if the digital image sensor is tilted, for example, from $l_1^{'}$ to $l_2^{'}$ the captured images would be changed depends on the tilt angles α and β of the sensor. In Fig. 4, we provide several cases of the effect to the images caused by sensor tilt of pinhole (perspective model) cameras and telecentric (affine model) cameras, from which we can distinguish the difference between the two imaging models.

To derive the imaging model of the bi-telecentric lens in Scheimpflug condition, we first assume that the camera sensor is installed perpendicular to the lens axis, and on this basis, characterize the Scheimpflug condition by introducing two tilt angles, α and β, which are the angles the sensor rotates around the horizontal and vertical axes, respectively.

2.2.1. Imaging model of an ideal bi-telecentric camera

Refer to Fig. 5, suppose a point $P(x, y, z)$ in the world coordinate is imaged on the camera sensor denoted as point $p(u_p, v_p)$. Its homogeneous image coordinate is projected from the camera coordinate in an affine form as

$$\begin{bmatrix} u_p \\ v_p \\ 1 \end{bmatrix} = \mathrm{A}P_C = \begin{bmatrix} m & 0 & u_0 \\ 0 & m & v_0 \\ 0 & 0 & 1 \end{bmatrix} \begin{bmatrix} x_c \\ y_c \\ 1 \end{bmatrix} \tag{1}$$

Here, m is the equivalent magnification of the telecentric lens. For an ideal telecentric camera, $e(u_0, v_0)$ is the image coordinate of the optical center, and u_0, v_0 can be set as zeros as there is no actual perspective center of a telecentric lens. For a particular system, there exists a unique world coordinate system. The pattern on the calibration board determines X and Y, as well as the original point O. The world and camera coordinate are related by a rotation matrix R and a translation vector t as

$$\begin{bmatrix} x_c \\ y_c \\ z_c \end{bmatrix} = \mathrm{R} \begin{bmatrix} x \\ y \\ z \end{bmatrix} + \mathrm{t} \tag{2}$$

Here, $\mathrm{R} = [\mathrm{r}_x \quad \mathrm{r}_y \quad \mathrm{r}_z]^T$ and $\mathrm{t} = [t_x \quad t_y \quad t_z]^T$. Because of the telecentricity in the image space, the variation of z_c will not change the image position as illustrated in Fig. 3 [3]. Therefore, the whole projection of a point in the world coordinate $P(x, y, z)$ to an image point $p(u_p, v_p)$ can be expressed as

$$\begin{bmatrix} \boldsymbol{p} \\ 1 \end{bmatrix} = \underbrace{\begin{bmatrix} m & 0 & u_0 \\ 0 & m & v_0 \\ 0 & 0 & 1 \end{bmatrix}}_{\mathrm{A}} \underbrace{\begin{bmatrix} r_{11} & r_{12} & r_{13} & t_x \\ r_{21} & r_{22} & r_{23} & t_y \\ 0 & 0 & 0 & 1 \end{bmatrix}}_{\mathrm{R_t}} \begin{bmatrix} \boldsymbol{P} \\ 1 \end{bmatrix} = \mathbf{H} \begin{bmatrix} \boldsymbol{P} \\ 1 \end{bmatrix} \tag{3}$$

Here, $\mathrm{H} = \mathrm{AR_t}$ is the homography matrix, transforming the world coordinates of objects into their corresponding image coordinates.

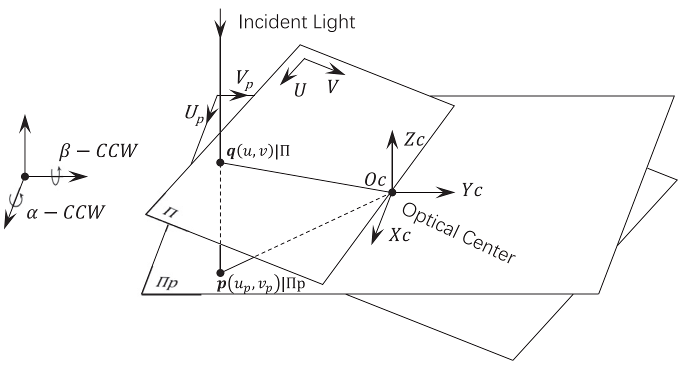

Fig. 6. The coordinate systems of the Scheimpflug bi-telecentric camera. The imaging coordinates of the tilted sensor are related to the ideal (not tilted) imaging coordinates by adding a rotation matrix based on α and β to the ideal bi-telecentric camera imaging model.

2.2.2. Imaging model of a Scheimpflug bi-telecentric camera

A camera sensor is a two-dimensional plane on which the image coordinates are located. The imaging coordinates of the tilted sensor, which corresponds to the captured image, can be related to the ideal (not tilted) imaging coordinates by adding a rotation matrix to the ideal bi-telecentric camera imaging model [28].

As shown in Fig. 6, plane Π is the sensor plane that intersects the optical axis at point O_C which is the optical center of the lens and O_C-$X_C Y_C Z_C$ is the coordinate system of the telecentric lens. Πp is the hypothesized ideal plane that also intersects the optical axis at point O_C and is perpendicular to Z_C axis. U_P-V_P and U-V are the pixel coordinate systems of plane Πp and Π, respectively. Suppose an incident light vertically irradiates plane Πp and respectively intersects plane Πp and Π at point $p(u_p, v_p)$ and $q(u, v)$. Since plane Πp is an auxiliary surface that does not exist, the relationship between plane Π and plane Πp can be bound by tilting plane Π around the Y_C axis and X_C axis successively. The tilt around the Z_C axis can be regarded as the lens's rotation, which does not affect the mathematical model of the imaging process.

The imaging coordinate $p(u_p, v_p)$ in Eq. (3) corresponds to the untilled plane Πp and can be considered as the intermediate transition variable. The ultimate pixel coordinate $q(u, v)$ is acquired by rotating $p(u_p, v_p)$ around Y_C axis with angle β and around X_C axis with angle α successively.

Refer to O_C-$X_C Y_C Z_C$ coordinate system, the rotation matrix is noted as R_{XY} and expressed as

$$R_{XY} = R_X R_Y = \begin{bmatrix} 1 & 0 & 0 \\ 0 & \cos\alpha & -\sin\alpha \\ 0 & \sin\alpha & \cos\alpha \end{bmatrix} \begin{bmatrix} \cos\beta & 0 & \sin\beta \\ 0 & 1 & 0 \\ -\sin\beta & 0 & \cos\beta \end{bmatrix} = \begin{bmatrix} \cos\beta & 0 & \sin\beta \\ \sin\alpha\sin\beta & \cos\alpha & -\sin\alpha\cos\beta \\ -\cos\alpha\sin\beta & \sin\alpha & \cos\alpha\cos\beta \end{bmatrix} \tag{4}$$

The unit direction vector of $(\mathbf{u_p}, \mathbf{v_p})$ in plane $\boldsymbol{\Pi}p$ are $\mathbf{u_p}(1, 0, 0)$ and $\mathbf{v_p}(0, 1, 0)$. After rotation by $\boldsymbol{R}_{XY}$ the unit direction vector of $\mathbf{u}$ and $\mathbf{v}$ in plane $\boldsymbol{\Pi}$ are

$$\begin{cases} u = \mathbf{R}_{XY}\mathbf{u_p} = \begin{bmatrix} \cos\boldsymbol{\beta} \\ \sin\boldsymbol{\alpha}\sin\boldsymbol{\beta} \\ -\cos\boldsymbol{\alpha}\sin\boldsymbol{\beta} \end{bmatrix} \\ v = \mathbf{R}_{XY}\mathbf{v_p} = \begin{bmatrix} 0 \\ \cos\boldsymbol{\alpha} \\ \sin\boldsymbol{\alpha} \end{bmatrix} \end{cases} \tag{5}$$

Taking pixel coordinates as the unit, $\boldsymbol{p}(\boldsymbol{u_p}, \boldsymbol{v_p})$ can be represented by $\boldsymbol{q}(\boldsymbol{u}, \boldsymbol{v})$ because the pixel coordinates of the optical center $\boldsymbol{O_C}$ in both planes are the same and can be regarded as $(\boldsymbol{u}_0, \boldsymbol{v}_0)$. Refer to $\boldsymbol{O_C}$-$\boldsymbol{X_C Y_C Z_C}$ coordinate system, the spatial coordinate of point $\boldsymbol{q}$ can be expressed as

$$\boldsymbol{u}(\boldsymbol{u} - \boldsymbol{u}_0) + \boldsymbol{v}(\boldsymbol{v} - \boldsymbol{v}_0) = \begin{bmatrix} \cos\boldsymbol{\beta} \\ \sin\boldsymbol{\alpha}\sin\boldsymbol{\beta} \\ -\cos\boldsymbol{\alpha}\sin\boldsymbol{\beta} \end{bmatrix}(\boldsymbol{u} - \boldsymbol{u}_0) + \begin{bmatrix} 0 \\ \cos\boldsymbol{\alpha} \\ \sin\boldsymbol{\alpha} \end{bmatrix}(\boldsymbol{v} - \boldsymbol{v}_0) \tag{6}$$

The coordinate values of point $\boldsymbol{q}$ in the $\boldsymbol{X_C}$ and $\boldsymbol{Y_C}$ directions are the same as point $\boldsymbol{p}$ because of the telecentricity so that the first two rows of Eq. (6) are the same to $(\boldsymbol{u_p} - \boldsymbol{u}_0, \boldsymbol{v_p} - \boldsymbol{v}_0)$:

$$\begin{cases} (\boldsymbol{u} - \boldsymbol{u}_0)\cos\boldsymbol{\beta} = \boldsymbol{u_p} - \boldsymbol{u}_0 \\ (\boldsymbol{u} - \boldsymbol{u}_0)\sin\boldsymbol{\alpha}\sin\boldsymbol{\beta} + (\boldsymbol{v} - \boldsymbol{v}_0)\cos\boldsymbol{\alpha} = \boldsymbol{v_p} - \boldsymbol{v}_0 \end{cases} \tag{7}$$

Based on Eq. (7), we can get the expression of $\boldsymbol{q}(\boldsymbol{u}, \boldsymbol{v})$ represented by $\boldsymbol{p}(\boldsymbol{u_p}, \boldsymbol{v_p})$ and $(\boldsymbol{\alpha}, \boldsymbol{\beta})$ as

$$\begin{bmatrix} \boldsymbol{u} \\ \boldsymbol{v} \\ 1 \end{bmatrix} = \begin{bmatrix} 1/\cos\boldsymbol{\beta} & 0 & \boldsymbol{u}_0 \\ -\tan\boldsymbol{\alpha}\tan\boldsymbol{\beta} & 1/\cos\boldsymbol{\alpha} & \boldsymbol{v}_0 \\ 0 & 0 & 1 \end{bmatrix} \begin{bmatrix} 1 & 0 & -\boldsymbol{u}_0 \\ 0 & 1 & -\boldsymbol{v}_0 \\ 0 & 0 & 1 \end{bmatrix} \begin{bmatrix} \boldsymbol{u_p} \\ \boldsymbol{v_p} \\ 1 \end{bmatrix} \tag{8}$$

By introducing Eq. (8) into Eq. (3), the final relationship between image point $\boldsymbol{q}(\boldsymbol{u}, \boldsymbol{v})$ and object point $\boldsymbol{P}(\boldsymbol{x}, \boldsymbol{y}, \boldsymbol{z})$ can be derived as

$$\begin{bmatrix} u \\ v \\ 1 \end{bmatrix} = \underbrace{\begin{bmatrix} m/\cos\beta & 0 & u_0 \\ -m\tan\alpha\tan\beta & m/\cos\alpha & v_0 \\ 0 & 0 & 1 \end{bmatrix}}_{\mathbf{A_m}} \underbrace{\begin{bmatrix} r_{11} & r_{12} & r_{13} & t_x \\ r_{21} & r_{22} & r_{23} & t_y \\ 0 & 0 & 0 & 1 \end{bmatrix}}_{\mathbf{R_t}} \begin{bmatrix} x \\ y \\ z \\ 1 \end{bmatrix} = \mathbf{H}\begin{bmatrix} \boldsymbol{P} \\ 1 \end{bmatrix} \tag{9}$$

Here, $\mathbf{H} = \mathbf{A_m R_t}$ is the new homography matrix. The only changed part is that the intrinsic matrix $\mathbf{A}$ becomes $\mathbf{A_m}$. The changes are equivalent to the magnification variation of $1/\cos\boldsymbol{\beta}$ and $1/\cos\boldsymbol{\alpha}$ in the two directions of the image coordinates, as well as an additional parameter$-\boldsymbol{m}\tan\boldsymbol{\alpha}\tan\boldsymbol{\beta}$ representing the tangential deformation. Compared with Peng's work [15], the tilt effect is simplified from tangential distortion to the intrinsic parameter changes, which is due to the orthogonality of the bi-telecentric optical path on both sides of the lens.

However, as Eq. (9) shows, there is an offset $(\boldsymbol{u}_0, \boldsymbol{v}_0)$ in $\mathbf{A_m}$. In fact, the telecentricity in the image space enables the offset $(\boldsymbol{u}_0, \boldsymbol{v}_0)$ be set any values because the optical center is located at infinity [7]. If the distortion of the bi-telecentric lens can be reduced to a negligible degree, we can move the origin of the camera coordinates $\boldsymbol{O_C}$ to the origin of the pixel coordinates. In the subsequent calibration, $(\boldsymbol{u}_0, \boldsymbol{v}_0)$ in $\mathbf{A_m}$ are set to zero in a distortion-free case to facilitate the calculation procedure.

It should be noted that if $\boldsymbol{\alpha}$ and $\boldsymbol{\beta}$ are reversed at the same time, $\mathbf{A_m}$ will not change, which means that there are two solutions of $\mathbf{A_m}$. This is also because of telecentricity in the image space. If It is necessary to analyze the effect of distortion, there are two ways to determine the signs, one is based on the involvement of the lens distortion model, and the other is based on the prior knowledge of the imaging system. However, the distortion of the lens may not provide enough perspective effect; thus, the signs can only be determined by the second way. In a specific system, the larger of the two tilt angles is easy to estimate, based on which the other tilt angle can be determined according to the sign constraint relationship of $-\boldsymbol{m}\tan\boldsymbol{\alpha}\tan\boldsymbol{\beta}$ in the retrieved $\mathbf{A_m}$.

3. Calibration of single Scheimpflug bi-telecentric camera

3.1. Simplified imaging model of a Scheimpflug bi-telecentric camera

As mentioned in the previous section, lens distortion is not considered in the intrinsic parameter calibration step, and $(\boldsymbol{u}_0, \boldsymbol{v}_0)$ can be set as any values. For convenience, we select the first pixel of the sensor as $(\boldsymbol{u}_0, \boldsymbol{v}_0)$ so that the perpendicular plane $\boldsymbol{\Pi}p$ can be regarded as being obtained by tilt the sensor plane $\boldsymbol{\Pi}$ around its first pixel by two angles $\boldsymbol{\alpha}$ and $\boldsymbol{\beta}$, as shown in Fig. 7. In this way, the intrinsic matrix is simply expressed as

$$\mathbf{A_m^S} = \begin{bmatrix} \boldsymbol{m}/\cos\boldsymbol{\beta} & 0 & 0 \\ -\boldsymbol{m}\tan\boldsymbol{\alpha}\tan\boldsymbol{\beta} & \boldsymbol{m}/\mathbf{cos}\boldsymbol{\alpha} & 0 \\ 0 & 0 & 1 \end{bmatrix} \tag{10}$$

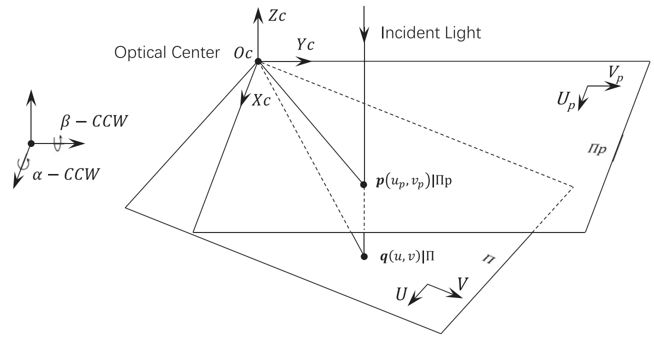

Fig. 7. The coordinate systems of the Scheimpflug bi-telecentric camera with $(\boldsymbol{u}_0, \boldsymbol{v}_0)$ being zeros.

Of course, $\boldsymbol{t_x}$ and $\boldsymbol{t_y}$ should be accordingly shifted to be homologous with the new $\boldsymbol{O_C}$. The imaging model thus becomes

$$\begin{bmatrix} u \\ v \\ 1 \end{bmatrix} = \underbrace{\begin{bmatrix} m/\cos\beta & 0 & 0 \\ -m\tan\alpha\tan\beta & m/\cos\alpha & 0 \\ 0 & 0 & 1 \end{bmatrix}}_{\mathbf{A_m^S}} \underbrace{\begin{bmatrix} r_{11} & r_{12} & r_{13} & t_x \\ r_{21} & r_{22} & r_{23} & t_y \\ 0 & 0 & 0 & 1 \end{bmatrix}}_{\mathbf{R_t}} \begin{bmatrix} x \\ y \\ z \\ 1 \end{bmatrix}$$
$$= \underbrace{\begin{bmatrix} h_{11} & h_{12} & h_{13} & h_{14} \\ h_{21} & h_{22} & h_{23} & h_{24} \\ 0 & 0 & 0 & 1 \end{bmatrix}}_{\mathbf{H}} \begin{bmatrix} \boldsymbol{P} \\ 1 \end{bmatrix} \tag{11}$$

3.2. The 2D planar calibration method

3.2.1. Intrinsic parameters calibration without lens distortion

The calibration board is placed in a specific posture to ensure that the whole plane is within the imaging depth of field to obtain a clear pattern image. After capturing the calibration pattern, the center coordinates of $\boldsymbol{N}$ circle markers are extracted by the ellipse fitting function. Because there is no perspective distortion, the ellipse center's bias does not need to be compensated [27]. The extracted center coordinates are noted as $\mathbf{p_c}$: $\boldsymbol{p}_1(\boldsymbol{u}_1, \boldsymbol{v}_1)$, $\boldsymbol{p}_2(\boldsymbol{u}_2, \boldsymbol{v}_2)$, $\cdots$ $\boldsymbol{p_N}(\boldsymbol{u_N}, \boldsymbol{v_N})$. The world coordinates system of each calibration posture is determined by its feature points, and the three-dimensional coordinate distribution of these feature points are correspondingly noted as $\mathbf{P_c}$: $\boldsymbol{P}_1(\boldsymbol{x}_1, \boldsymbol{y}_1, 0)$, $\boldsymbol{P}_2(\boldsymbol{x}_2, \boldsymbol{y}_2, 0)$, $\cdots$ $\boldsymbol{P_N}(\boldsymbol{x_N}, \boldsymbol{y_N}, 0)$. Because the $\boldsymbol{z}$ of each point is zero so that $\mathbf{P_c}$ is shorted as $\mathbf{P_c^S} = (\boldsymbol{x_i}, \boldsymbol{y_i})$ and $\mathbf{R_t}$ is shorted as $\mathbf{R_t^S}$

$$\mathbf{R_t^S} = \begin{bmatrix} \boldsymbol{r}_{11} & \boldsymbol{r}_{12} & \boldsymbol{t_x} \\ \boldsymbol{r}_{21} & \boldsymbol{r}_{22} & \boldsymbol{t_y} \\ 0 & 0 & 1 \end{bmatrix} \tag{12}$$

Therefore, the imaging model of the calibration pattern is further simplified as

$$\begin{bmatrix} u_i \\ v_i \\ 1 \end{bmatrix} = \underbrace{\begin{bmatrix} j & 0 & 0 \\ l & k & 0 \\ 0 & 0 & 1 \end{bmatrix}}_{\mathbf{A_m^S}} \underbrace{\begin{bmatrix} r_{11} & r_{12} & t_x \\ r_{21} & r_{22} & t_y \\ 0 & 0 & 1 \end{bmatrix}}_{\mathbf{R_t^S}} \begin{bmatrix} x_i \\ y_i \\ 1 \end{bmatrix} = \underbrace{\begin{bmatrix} h_{11} & h_{12} & h_{14} \\ h_{21} & h_{22} & h_{24} \\ 0 & 0 & 1 \end{bmatrix}}_{\mathbf{H^S}} \begin{bmatrix} \mathbf{P_c^S} \\ 1 \end{bmatrix} \tag{13}$$

with

$$\begin{cases} j = \boldsymbol{m}/\cos\boldsymbol{\beta} \\ k = \boldsymbol{m}/\cos\boldsymbol{\alpha} \\ l = -m\tan\boldsymbol{\alpha}\tan\boldsymbol{\beta} \end{cases} \tag{14}$$

The parameters can be solved in three steps: Step 1. Calculate the homography matrix; Step 2. Solve $\boldsymbol{j}$, $\boldsymbol{k}$, and $\boldsymbol{l}$ according to the unit orthogonality of the rotation matrix, and Step 3. Get $\boldsymbol{\alpha}$ and $\boldsymbol{\beta}$ from $\boldsymbol{j}$, $\boldsymbol{k}$, and $\boldsymbol{l}$. The last step is to verify whether the calibrated result is consistent with the actual system and is unnecessary for subsequent stereo rectification.

Step 1. Calculate the homography matrix

This step is to solve $\boldsymbol{h}_{11}$, $\boldsymbol{h}_{12}$, $\boldsymbol{h}_{21}$, and $\boldsymbol{h}_{22}$ in $\mathbf{H^S}$. The relationship between the world coordinates $(\boldsymbol{x_i}, \boldsymbol{y_i})$ of each feature point and its pixel coordinates $(\boldsymbol{u_i}, \boldsymbol{v_i})$ in the image provides two equations as shown in Eq. (15). Since three non-collinear points determine a plane, the rank of the augmented coefficient matrix derived from all the points on a plane is six; thus, the solution to Eq. (15) provided by all points in a calibration pattern exists. All the six variables in $\mathbf{H^S}$ can be solved directly by using the least square method [3].

$$\begin{bmatrix} \boldsymbol{x}_1 & \boldsymbol{y}_1 & 1 & 0 & 0 & 0 \\ 0 & 0 & 0 & \boldsymbol{x}_1 & \boldsymbol{y}_1 & 1 \\ \vdots & \vdots & \vdots & \vdots & \vdots & \vdots \\ \boldsymbol{x_N} & \boldsymbol{y_N} & 1 & 0 & 0 & 0 \\ 0 & 0 & 0 & \boldsymbol{x_N} & \boldsymbol{y_N} & 1 \end{bmatrix} \begin{bmatrix} \boldsymbol{h}_{11} \\ \boldsymbol{h}_{12} \\ \boldsymbol{h}_{14} \\ \boldsymbol{h}_{21} \\ \boldsymbol{h}_{22} \\ \boldsymbol{h}_{24} \end{bmatrix} = \begin{bmatrix} \boldsymbol{u}_1 \\ \boldsymbol{v}_1 \\ \vdots \\ \boldsymbol{u_N} \\ \boldsymbol{v_N} \end{bmatrix} \tag{15}$$

Step 2. Solve $\boldsymbol{j}$, $\boldsymbol{k}$, and $\boldsymbol{l}$ according to the unit orthogonality of the rotation matrix

First, we need to express the rotation parameters $(\boldsymbol{r}_{11}, \boldsymbol{r}_{12}, \boldsymbol{r}_{21}, \boldsymbol{r}_{22})$ as the relationship between $(\boldsymbol{h}_{11}, \boldsymbol{h}_{12}, \boldsymbol{h}_{21}, \boldsymbol{h}_{22})$ and $(\boldsymbol{j}, \boldsymbol{k}, \boldsymbol{l})$. Based on Eq. (13) we can write $\mathbf{R_t^S}$ as

$$\mathbf{R_t^S} = \mathbf{A_m^{S^{-1}}}\mathbf{H^S} = \begin{bmatrix} 1/\boldsymbol{j} & 0 & 0 \\ -\boldsymbol{l}/\boldsymbol{jk} & 1/\boldsymbol{k} & 0 \\ 0 & 0 & 1 \end{bmatrix} \begin{bmatrix} \boldsymbol{h}_{11} & \boldsymbol{h}_{12} & \boldsymbol{h}_{14} \\ \boldsymbol{h}_{21} & \boldsymbol{h}_{22} & \boldsymbol{h}_{24} \\ 0 & 0 & 1 \end{bmatrix} \tag{16}$$

So that

$$\begin{cases} \boldsymbol{r}_{11} = \boldsymbol{h}_{11}/\boldsymbol{j} \\ \boldsymbol{r}_{12} = \boldsymbol{h}_{12}/\boldsymbol{j} \\ \boldsymbol{r}_{21} = \boldsymbol{h}_{21}/\boldsymbol{k} - \boldsymbol{h}_{11}\boldsymbol{l}/\boldsymbol{jk} \\ \boldsymbol{r}_{22} = \boldsymbol{h}_{22}/\boldsymbol{k} - \boldsymbol{h}_{12}\boldsymbol{l}/\boldsymbol{jk} \end{cases} \tag{17}$$

Then the unit orthogonality of $\mathbf{R}$ is applied, that is

$$\begin{cases} \langle \mathbf{r_x}, \mathbf{r_x} \rangle = 1 \\ \langle \mathbf{r_y}, \mathbf{r_y} \rangle = 1 \\ \langle \mathbf{r_x}, \mathbf{r_y} \rangle = 0 \end{cases} \tag{18}$$

After substituting Eq. (17) into Eq. (18) and combining similar terms, we can get a simplified equation as

$$\boldsymbol{j}^2\boldsymbol{k}^2 - \left(\boldsymbol{k}^2 + \boldsymbol{l}^2\right)\left(\boldsymbol{h}_{11}^2 + \boldsymbol{h}_{12}^2\right) - \boldsymbol{j}^2\left(\boldsymbol{h}_{21}^2 + \boldsymbol{h}_{22}^2\right) + 2\boldsymbol{jl}\left(\boldsymbol{h}_{11}\boldsymbol{h}_{21} + \boldsymbol{h}_{12}\boldsymbol{h}_{22}\right)$$
$$+\left(\boldsymbol{h}_{12}\boldsymbol{h}_{21} - \boldsymbol{h}_{11}\boldsymbol{h}_{22}\right)^2 = 0 \tag{19}$$

It can be written as follows

$$\begin{bmatrix} 1 & -\left(h_{11}^2 + h_{12}^2\right) & -\left(h_{21}^2 + h_{22}^2\right) & 2\left(h_{11}h_{21} + h_{12}h_{22}\right) \end{bmatrix} \underbrace{\begin{bmatrix} j^2k^2 \\ k^2 + l^2 \\ j^2 \\ jl \end{bmatrix}}_{\mathbf{S}}$$
$$= -\left(h_{12}h_{21} - h_{11}h_{22}\right)^2 \tag{20}$$

Note that there are four unknowns in $\mathbf{S}(s_1, s_2, s_3, s_4)$ with $s_1 = \boldsymbol{j}^2\boldsymbol{k}^2$, $s_2 = \boldsymbol{k}^2 + \boldsymbol{l}^2$, $s_3 = \boldsymbol{j}^2$, and $s_4 = \boldsymbol{jl}$. Therefore, at least four sets of calibration images are required to solve $\mathbf{S}$. After $\mathbf{S}$ is solved, four equations containing three unknown internal parameters are obtained. The ***Levenberg-Marquardt*** algorithm is applied here to get the optimized results. Because the magnification $\boldsymbol{m}$ is a negative value and absolute values of $\boldsymbol{\alpha}$ and $\boldsymbol{\beta}$ are less than 90°, the sign of $\boldsymbol{j}$, $\boldsymbol{k}$, and $\boldsymbol{l}$ can be determined based on $\boldsymbol{S}(s_1, s_2, s_3, s_4)$. The initial value of $\boldsymbol{j}$, $\boldsymbol{k}$, and $\boldsymbol{l}$ for

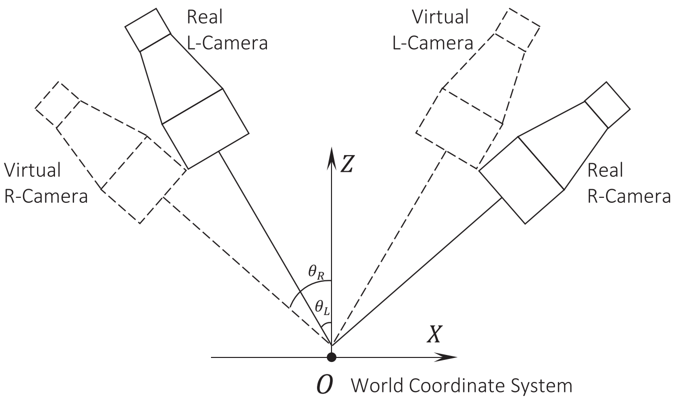

Fig. 8. The lens posture ambiguities of a stereo telecentric system. For a specific world coordinate system, due to the lens's telecentricity, there exist two possible solutions for a single camera.

iteration can be calculated by

$$\begin{cases} j_0 = -\sqrt{s_3} \\ k_0 = -\sqrt{s_1/s_3} \\ l_0 = -\frac{s_4}{\sqrt{s_3}} \end{cases} \tag{21}$$

The objective function F_{opt}^1 of the *Levenberg-Marquardt* algorithm is

$$F_{opt}^1 = \underset{j,k,l}{\operatorname{argmin}} \sum \left\| \mathbf{F} - \mathbf{S}^2 \right\| \tag{22}$$

with $\mathbf{F} = [j^2k^2, k^2 + l^2, j^2, jl]^{\mathrm{T}}$ and $\mathbf{S} = [s_1, s_2, s_3, s_4]^{\mathrm{T}}$.

Step 3. Get m, α and β from j, k, and l

Refer to Eq. (14), we can derive that

$$(k/j)^2\cos^4\alpha - \left((l/j)^2 + (k/j)^2 + 1\right)\cos^2\alpha + 1 = 0 \tag{23}$$

By solving Eq. (23), the rotation angle α can be acquired, and then β can also be obtained based on Eq. (14). The calcualted angle will be compared with the physical angles of the camera lens to make sure that the imaging process is correctly modeled.

3.2.2. Extrinsic parameters

After the intrinsic parameters are obtained, $\mathbf{R}_{2\times 2}$ (r_{11}, r_{12}, r_{21}, r_{22}) of each calibration pattern can be calculated by Eq. (17). Because $\mathbf{R}$ is unitary and orthogonal, the remaining elements of $\mathbf{R}$ can be calculated through

$$\begin{cases} r_{13} = \pm\sqrt{1 - r_{11}^2 - r_{12}^2} \\ r_{23} = \pm\sqrt{1 - r_{21}^2 - r_{22}^2} \\ \mathbf{r}_z = \mathbf{r}_x \times \mathbf{r}_y \end{cases} \tag{24}$$

However, the derived rotation matrix is not strictly orthogonal and needs to be orthogonalized using SVD for further optimization. Furthermore, the telecentricity of the plane imaging process has its natural disadvantage that the posture of the lens has ambiguities [24], which could lead to wrong 3D results based on a stereo telecentric system, as shown in Fig. 8. For the chosen world coordinate system, the ***L-camera*** can be either the ***real camera*** or the ***virtual camera***. The calibration pattern represented by the world coordinate system is recorded with exactly the same image by the two cameras. It is the same situation for the ***R-camera***, so the stereo structure cannot be uniquely determined. This problem is actually originated from Eq. (24) that both r_{13} and r_{23} have positive and negative solutions.

To solve this problem, we adopt the method proposed by Chen [7] that uses a micro-positioning stage to provide a known translational displacement z_d along the Z axis of the world coordinate system so that signs of r_{13} and r_{23} can be confirmed. Together with the captured image before the displacement, the signs of r_{31} and r_{32} can be unambiguously determined before the subsequent optimization. For a stereo telecentric system, only one calibration posture needs to be captured by two cameras at the same time to eliminate its ambiguity of external parameters, and this calibration pose is used as the shared world coordinates for the two cameras.

3.2.3. Global optimization considering lens distortion

Without considering the lens distortion, we have got the closed-form solutions of the parameters in Eq. (13). However, two problems still need taking into account. The first one is that the derived rotation matrix from Eq. (24) is not strictly orthogonal. The second one is that lens distortion has not been calibrated. In this subsection, two non-linear optimization processes are conducted in sequence to solve these problems. The optical center $e(u_0, v_0)$ needs to be explicit to ack as the distortion center, therefore the derived $\mathbf{A}_{\mathbf{m}}^{\mathbf{S}}$ and $\mathbf{R}_{\mathbf{t}}^{\mathbf{S}}$ needs to be respectively adjusted to Eq. (25) to keep $\mathbf{H}^{\mathbf{S}}$ the same as in Eq. (13).

$$\begin{cases} \mathbf{A}_{\mathbf{m}} = \begin{bmatrix} j & 0 & u_0 \\ l & k & v_0 \\ 0 & 0 & 1 \end{bmatrix} \\ \mathbf{R}_{\mathbf{t}}^{\mathbf{S}} = \begin{bmatrix} r_{11} & r_{12} & t_x - (u_0/j) \\ r_{21} & r_{22} & t_y - (v_0/j) \\ 0 & 0 & 1 \end{bmatrix} \end{cases} \tag{25}$$

The initial values of the optical center (distortion center) $e(u_0, v_0)$ can be set as the sensor center or derived by the optical center estimation algorithm [38]. The first non-linear optimization is to update the unique intrinsic matrix $\mathbf{A}_{\mathbf{m}}$ from different calibration postures as well as each orthogonal rotation matrix $\mathbf{R}$ and translation vector $\mathbf{t}$ by minimizing the following function with *Levenberg-Marquardt* algorithm:

$$F_{opt}^2 = \underset{\mathbf{A}_{\mathbf{m}},\mathbf{R},\mathbf{t}}{\operatorname{argmin}} \sum_{\xi} \sum_{\eta} \|\mathbf{q}_{\xi,\eta} - \hat{\mathbf{q}}(\mathbf{A}_{\mathbf{m}}, \mathbf{R}_{\xi}, \mathbf{t}_{\xi}, \mathbf{P}_{\xi,\eta})\|^2 \tag{26}$$

Here, ξ is the number of calibration postures, η is the number of feature points on the calibration pattern, $\mathbf{q}_{\xi,\eta}$ and $\mathbf{P}_{\xi,\eta}$ are the control points on the captured images and the calibration pattern, respectively. $\hat{\mathbf{q}}$ is the projection of feature points $\mathbf{P}_{\xi,\eta}$ according to Eq. (13). In the optimization process, the rotation matrix $\mathbf{R}$ is firstly transformed into an orthogonal matrix using SVD and then parameterized by three scalers using *Rodrigues' rotation formula*.

When F_{opt}^2 is minimized, the generated intrinsic matrix $\mathbf{A}_{\mathbf{m}}$ and extrinsic matrix $\mathbf{R}_{\mathbf{t}}^{\mathbf{S}}$ are utilized to calculate the initial guesses of distortion coefficients in another non-linear optimization. Traditional camera distortion includes radial distortion and tangential distortion. Since the effect of tangential distortion can be alternatively represented by a part of the Schiempflug condition, the distortion needs to be compensated only contains three radial coefficients denoted as $\mathbf{k} = [\ k_1 \quad k_2 \quad k_3\ ]$ and can be modeled in the camera coordinates system as

$$\begin{cases} \begin{bmatrix} x_c^d \\ y_c^d \end{bmatrix} = \begin{bmatrix} x_c^u \\ y_c^u \end{bmatrix} + \begin{bmatrix} \delta_x \\ \delta_y \end{bmatrix}, \\ \begin{bmatrix} \delta_x \\ \delta_y \end{bmatrix} = \begin{bmatrix} x_c^u r_c^2 & x_c^u r_c^4 & x_c^u r_c^6 \\ y_c^u r_c^2 & y_c^u r_c^4 & y_c^u r_c^6 \end{bmatrix} [\ k_1 \quad k_2 \quad k_3\ ]^T \end{cases} \tag{27}$$

Here, (x_c^d, y_c^d) and (x_c^u, y_c^u) are the distorted and undistorted positions in the camera coordinate system. $r_c^2 = x_c^{u^2} + y_c^{u^2}$. Based on the optimized results from Eq. (26), we can derive the initial value of $\mathbf{k}$ by solving Eq. (27) with

$$\begin{cases} [\ x_c^d \quad y_c^d \quad 1\ ]^T = \mathbf{A}_{\mathbf{m}}^{-1} [\ u_c \quad v_c \quad 1\ ]^T \\ [\ x_c^u \quad y_c^u\ ]^T = \mathbf{R}_{\mathbf{t}}^{\mathbf{S}} [\ x \quad y \quad 1\ ]^T \end{cases} \tag{28}$$

Then the following non-linear optimization can be performed to refine all the parameters with the following cost function:

$$F_{opt}^3 = \frac{\operatorname{argmin}}{\mathbf{A}_{\mathbf{m}}, \mathbf{R}, \mathbf{t}, \mathbf{k}} \sum_{\xi} \sum_{\eta} \left\| \mathbf{q}_{\xi,\eta} - \hat{\mathbf{q}}(\mathbf{A}_{\mathbf{m}}, \mathbf{R}_{\xi}, \mathbf{t}_{\xi}, \mathbf{k}, \mathbf{P}_{\xi,\eta}) \right\|^2 \tag{29}$$

Here, $\hat{\mathbf{q}}$ is the new projection of the feature point $\mathbf{P}_{\xi,\eta}$ according to Eq. (13) with the updated camera coordinate in Eq. (27). After F_{opt}^3 is minimized, the calibration of a telecentric camera is thoroughly completed.

4. Stereo rectification of Scheimpflug telecentric lenses for stereo-matching

As we know that 3D measurement or reconstruction relies on multi-view information, which usually needs to be extracted by means such as fringe phase-matching or intensity feature correlation. The phase-matching methods calculate the phase distribution map from the captured sinusoidal fringe patterns, and based on a reverse calibration procedure of a projector's optical path, then directly finds the matching point between the projector and the camera according to the phase values [17,39,40]. The intensity correlation methods search the matching point by correlating the intensities around the source point with the intensities around the candidate points in the other image through specific routines [34] without the necessity to calibrate a projector. The recently proposed microscopic telecentric stereo vision system [3] combines the advantages of the two kinds of methods. The critical stage is that the stereo rectification renders the phase stereo matching between cameras be much more efficient and convenient.

The epipolar geometry of two telecentric cameras is similar to that of two pinhole cameras [41–43]. An undistorted pixel $p_L(u_L, v_L)$ in the left view corresponds to an epipolar line in the other view, on which the matched pixel $p_R(u_R, v_R)$ meets the affine epipolar constraint equation as

$$au_R + bv_R + cu_L + dv_L + e = 0 \tag{30}$$

where $a \sim e$ are five constants. The original images need to be transformed into new ones, and thus new sets of camera parameters are acquired. Different from calculating the fundamental matrix between two views, we first calibrate the cameras with two sets of parameters for each camera and then undistort them in the image coordinate, at last, rectify them with the newly derived imaging models. Here we use a prime to represent the new parameters and add subscript L or R to distinguish the left and right cameras. Then we describe the original projection process for both cameras as

$$\begin{cases} \begin{bmatrix} p_L \\ 1 \end{bmatrix} = \mathbf{A}_{mL}\mathbf{R}_{tL}\begin{bmatrix} P \\ 1 \end{bmatrix} = \mathbf{H}_L\begin{bmatrix} P \\ 1 \end{bmatrix} \\ \begin{bmatrix} p_R \\ 1 \end{bmatrix} = \mathbf{A}_{mR}\mathbf{R}_{tR}\begin{bmatrix} P \\ 1 \end{bmatrix} = \mathbf{H}_R\begin{bmatrix} P \\ 1 \end{bmatrix} \end{cases} \tag{31}$$

And the rectified projection process for both cameras as

$$\begin{cases} \begin{bmatrix} p'_L \\ 1 \end{bmatrix} = \mathbf{A}'_{mL}\mathbf{R}'_{tL}\begin{bmatrix} P \\ 1 \end{bmatrix} = \mathbf{H}'_L\begin{bmatrix} P \\ 1 \end{bmatrix} \\ \begin{bmatrix} p'_R \\ 1 \end{bmatrix} = \mathbf{A}'_{mR}\mathbf{R}'_{tR}\begin{bmatrix} P \\ 1 \end{bmatrix} = \mathbf{H}'_R\begin{bmatrix} P \\ 1 \end{bmatrix} \end{cases} \tag{32}$$

The final goal is to ensure that each object point will be imaged on the same row in their own rectified image. To minimize the loss of invalid areas of the rectified images, we design new imaging models as possible as close to the original parameters. For this purpose, three criteria are drawn as the following:

1. Remain the optical axis direction ($\mathbf{r}'_{zL}$ and $\mathbf{r}'_{zR}$) unchanged;
2. Ensure that the y direction of the rotation matrixes ($\mathbf{r}'_{yL}$ and $\mathbf{r}'_{yR}$) are the same because the disparity is distributed in the x_c direction.
3. To prevent the tilt component (l in $\mathbf{A}_m$) from affecting our final goal, we can remove l and then average other parameters in $\mathbf{A}_{mL}$ and $\mathbf{A}_{mR}$ to generate a common $\mathbf{A}'^{S}_{m}$ to serve two camera models.

$$\mathbf{A}'_{mL} = \mathbf{A}'_{mR} = \begin{bmatrix} (j_L + j_R)/2 & 0 & u_0 \\ 0 & (k_L + k_R)/2 & v_0 \\ 0 & 0 & 1 \end{bmatrix} \tag{33}$$

According to the above criteria, the new direction vector of the camera's optical axes $\mathbf{r}'_{zL}$ and $\mathbf{r}'_{zR}$ remain unchanged and should intersect with each other in a plane, which is realized by setting appropriate $\mathbf{t}'_L$ and $\mathbf{t}'_R$. $\mathbf{r}'_{yL}$ and $\mathbf{r}'_{yR}$ should be perpendicular to this plane so that the disparity only appears in the horizontal direction ($\mathbf{r}'_{xL}$ and $\mathbf{r}'_{xR}$). Therefore, the new rotation matrix $\mathbf{R}'_L$ and $\mathbf{R}'_R$ is derived through

$$\begin{cases} \mathbf{r}'_{zL} = r_{zL} \\ \mathbf{r}'_{zR} = r_{zR} \end{cases} \tag{34}$$

r'_{yL} and $\mathbf{r}'_{yR}$ should be perpendicular to both $\mathbf{r}'_{zL}$ and $\mathbf{r}'_{zR}$.

$$\begin{cases} \mathbf{r}'_{yL} = norm(\mathbf{r}'_{zL} \times \mathbf{r}'_{zR}) \\ \mathbf{r}'_{yR} = \mathbf{r}'_{yL} \end{cases} \tag{35}$$

Finally, based on the orthogonality of the rotation matrix, $\mathbf{r}'_{xL}$ and $\mathbf{r}'_{xR}$ can be obtained as

$$\begin{cases} \mathbf{r}'_{xL} = \mathbf{r}'_{zL} \times \mathbf{r}'_{yL} \\ \mathbf{r}'_{xR} = \mathbf{r}'_{zR} \times \mathbf{r}'_{yR} \end{cases} \tag{36}$$

Where, function "norm" stands for the normalization of a matrix and operator "×" stands for the cross product. The requirement to $\mathbf{t}'_L$ and $\mathbf{t}'_R$ is $\mathbf{t}'_{yL} = \mathbf{t}'_{yR}$ to disappear the vertical disparity. Here we first derive an intermediate translation vector as

$$\begin{cases} \begin{bmatrix} \tau_{xL} & \tau_{yL} & 1 \end{bmatrix}^T = \mathbf{R}'_L\mathbf{R}_L^{-1}\begin{bmatrix} t_{xL} & t_{yL} & 1 \end{bmatrix}^T \\ \begin{bmatrix} \tau_{xR} & \tau_{yR} & 1 \end{bmatrix}^T = \mathbf{R}'_R\mathbf{R}_R^{-1}\begin{bmatrix} t_{xR} & t_{yR} & 1 \end{bmatrix}^T \end{cases} \tag{37}$$

By setting the new translation vector as

$$\begin{cases} t'_{xL} = \tau_{xL} \\ t'_{xR} = \tau_{xR} \\ t'_{yL} = t'_{yR} = (\tau_{yL} + \tau_{yR})/2 \end{cases} \tag{38}$$

The new translation vectors $\mathbf{t}'_L$ and $\mathbf{t}'_R$ are obtained. For now, we have derived all the parameters to generate $\mathbf{H}'_L$ and $\mathbf{H}'_R$. Therefore, the transformation between the rectified and the original image coordinates can be executed by

$$\begin{cases} \begin{bmatrix} p'_L \\ 1 \end{bmatrix} = \mathbf{H}'_L\mathbf{H}_L^{+}\begin{bmatrix} p_L \\ 1 \end{bmatrix} \\ \begin{bmatrix} p'_R \\ 1 \end{bmatrix} = \mathbf{H}'_R\mathbf{H}_R^{+}\begin{bmatrix} p_R \\ 1 \end{bmatrix} \end{cases} \tag{39}$$

And vice versa. The symbol "+" means pseudo-inverse of a matrix. However, it should be noted again that the rectification is valid under the distortion-free situation. Thus, before the rectification, the lens distortion should be correctly removed by the accurate calibration of the cameras.

5. Experiments

5.1. Single-camera calibration in Scheimpflug condition

First, To verify the correctness of the imaging model containing the tilt angle information of the sensor in Eq. (11), we adjusted the inclination of a telecentric camera to five different angles along the sensor's long side. As shown in Fig. 9, the camera used in our experiment is an ***Imaging Source DMK*** 33***US***183 camera equipped with a ***SONY IMX***183***CLK*** sensor that has a pixel size p_s of 2.4 μm and maximum resolution of 5544 × 3694. The lens is ***TCSM***048 from ***Opto-Engineering*** with a working distance of 134.6 mm and a vertical magnification varying from 0.133 to 0.185, depending on the inclination angle. The FOV of the lens on the detector side can reach 2/3 inches, which is larger than the sensor size, so in order to fully apply the lens FOV, we set the image resolution as 4096 × 2160.

The working distance is controlled to 134.6 mm to minimize the influence of distortion. The sensor plane behind the lens is adjusted by controlling the screwed amount of the lens thread into the adapter socket

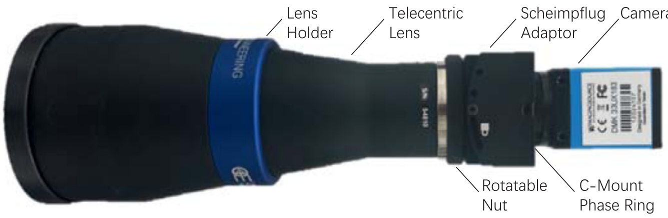

Fig. 9. The picture of the Scheimpflug telecentric camera in the calibration experiment.

to assure the best imaging quality. A freely rotatable nut on the outside of the lens thread is used to lock the lens and the adapter. Note that the relative phase between the camera interface and the Scheimpflug adaptor can also be adjusted by unlocking the connecting clasp, so it is somehow tricky to ensure that the sensor only has an α angle. Still, more or less a small β angle exists (manually controlled within $\pm 1^{\circ}$).

The calibration target is a special visual calibration board made of glass material with an external dimension of 25 mm × 25 mm, as shown in Fig. 10(a). The pattern consists of a 31 × 27 array of circles with a diameter of 0.323 mm, and the distance between the centers of every two circles is 0.645 mm. Through circle extraction, center positioning, and sorting, as shown in Fig. 10(b), each image can provide 31 × 27 feature points, as shown in Fig. 10(c).

The tilt angle of the Scheimpflug adaptor is respectively set to 0°, 5°, 10°, 15°, and 20°. At each angle, ten calibration images are captured by arranging the calibration board in ten different postures. The calculated intrinsic matrix $\mathbf{A}_{\mathbf{m}}^{\mathbf{S}}$ and the retrieved (α, β) are listed in Table 1. The equivalent magnification m_e is calculated through Eq. (14) and the optical magnification m_o is derived by multiplying the equivalent magnification m_e with the pixel size p_s. For each tilt angle, the intrinsic matrix $\mathbf{A}_{\mathbf{m}}^{\mathbf{S}}$ contains three valid values termed j, k, and l. From the results we can see that the retrieved α and β are quite close to the preset angles, which experimentally proves the effectiveness of the proposed calibration method. However, due to the mechanical error caused by manual operation, there are ± 0.5 degrees bias between the preset and retrieved angles. The retrieved optical magnification m_o of all situations are the same to the specified magnification (0.185) even though the equivalent magnification m_e varies a little bit.

We also use another two calibration models and algorithms to analyze the extracted calibration data, namely the orthogonal telecentric model and the perspective pinhole model. The intrinsic matrixes and reprojection errors are listed in Table 2. The reprojection errors in u and v direction with tilt angle change is shown in Fig. 13. With the orthogonal telecentric model, a consistent internal matrix of the camera should be solved based on each calibration pattern. However, with the data acquired under the Scheimpflug condition, the equivalent magnification differs between two axes and postures. Though the final internal matrix can only be obtained by iterative optimization, the calibration error still is bigger than that of our method because the tangential parameter is lost. If a tangential value is added to the intrinsic matrix, a similar result can be obtained from our method. However, the physical meaning of this variable refers to the production defect of the sensor, which often takes a tiny value so that the larger tangential value calculated from the data acquired in Scheimpflug condition is inapplicable. In addition, a significant deviation between the magnification in two axes does not accord with the orthogonal telecentric model.

For the pinhole model, the difference with the telecentric model is that it has a scaling factor s. The equivalent focal length of the perspective model is quite long to be approximated as a telecentric model. A large equivalent focal length corresponds to a large distance of the optical center from the sensor surface. Due to sensor tilt, it is necessary to set different equivalent focal lengths in two axial directions. From the calibration result shown in Table 2. In some cases, it matches better in the reprojection error than the orthogonal telecentric model because the tilt effect is offset by the difference in the axial focal lengths. However, if β tilt is involved, another tangential parameter must be considered. Overall, the comparison proves that our method constructs a more reasonable model with minimum error under variable cases.

To intuitively show the recovered posture of the sensor after rotation around $\mathbf{u_p}$ and $\mathbf{v_p}$ axis, we plot the sensor planes in camera space as shown in Fig. 11, as well as the oblique, top, front, and side views of the planes retrieved in five cases. The black rectangle is the untilted sensor plane, while the blue rectangle is the tilt sensor plane. For a more apparent distinction between the two planes, the untilted sensor plane is placed in a lower position. It can be clearly seen from the front view that the tilt angle increases gradually with the increase of the actual preset angle. Correspondingly, the top view and side view also changes as the sensor plane gets more and more sloping.

The lens distortion is then considered by introducing the lens distortion center estimation and iterated through Eq. (29). However, the distortion parameters are relatively tiny and converged to different values. Besides, neither the re-projection errors nor the calibration results show an apparent difference between considering and without considering distortion. The reason may be that the distortion of the lens is so small that its effect is even overwhelmed by the noise of the images.

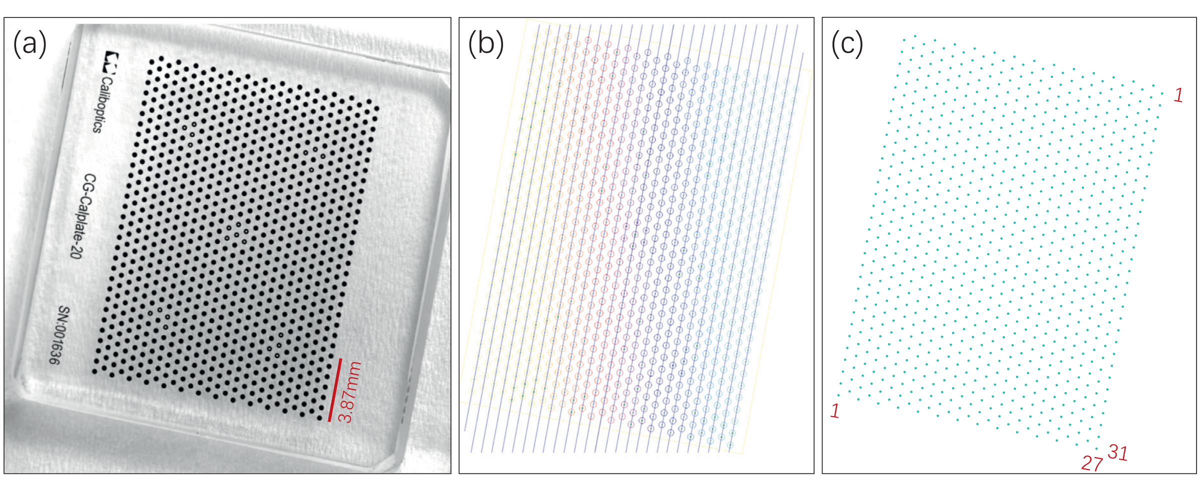

Fig. 10. (a) Calibration board; (b) feature points in sorting; (c) extracted feature points.

Table 1
The calculated intrinsic matrix and relative parameters from five situations with increasing preset tilt angles.

Set tilt angles	$\mathbf{A}_{\mathrm{m}}^{\mathrm{S}}$	α	β	m_e(equivalent)	m_o(optical)
$\alpha = 0° \ \beta = 0°$	$\begin{bmatrix} -76.7146 & 0 & 0 \\ 0.0088 & -76.7153 & 0 \\ 0 & 0 & 1 \end{bmatrix}$	0.6366°	0.5920°	−76.7105	−0.1841
$\alpha = 5° \ \beta = 0°$	$\begin{bmatrix} -76.7137 & 0 & 0 \\ 0.0348 & -77.0143 & 0 \\ 0 & 0 & 1 \end{bmatrix}$	5.0725°	0.2931°	−76.7127	−0.1841
$\alpha = 10\,° \beta = 0°$	$\begin{bmatrix} -76.7200 & 0 & 0 \\ 0.1662 & -77.9366 & 0 \\ 0 & 0 & 1 \end{bmatrix}$	10.1606°	0.6927°	−76.7144	−0.1841
$\alpha = 15\,° \beta = 0°$	$\begin{bmatrix} -76.7301 & 0 & 0 \\ 0.3105 & -79.5690 & 0 \\ 0 & 0 & 1 \end{bmatrix}$	15.3736°	0.8434°	−76.7218	−0.1841
$\alpha = 20\,° \beta = 0°$	$\begin{bmatrix} -76.7281 & 0 & 0 \\ 0.3779 & -81.2584 & 0 \\ 0 & 0 & 1 \end{bmatrix}$	19.2388°	0.8087°	−76.7204	−0.1841

Table 2
The intrinsic matrixes derived from three models under five tilt angles.

Set tilt angle	Orthogonal telecentric model	Reprojection error	Perspective pinhole model	Reprojection error
$\alpha = 0° \ \beta = 0°$	$\begin{bmatrix} -76.7157 & 0 & 0 \\ 0 & -76.7163 & 0 \\ 0 & 0 & 1 \end{bmatrix}$	(0.0603, 0.0591)	$s\begin{bmatrix} 3.634\mathbf{e}^{6} & 0 & 2047.5 \\ 0 & 3.618\mathbf{e}^{6} & 1079.5 \\ 0 & 0 & 1 \end{bmatrix}$	(0.0939, 0.0966)
$\alpha = 5° \ \beta = 0°$	$\begin{bmatrix} -76.7167 & 0 & 0 \\ 0 & -77.0093 & 0 \\ 0 & 0 & 1 \end{bmatrix}$	(0.0881, 0.0877)	$s\begin{bmatrix} 1.981\mathbf{e}^{6} & 0 & 2047.5 \\ 0 & 2.086\mathbf{e}^{6} & 1079.5 \\ 0 & 0 & 1 \end{bmatrix}$	(0.1297, 0.1079)
$\alpha = 10\,° \beta = 0°$	$\begin{bmatrix} -76.7117 & 0 & 0 \\ 0 & -77.9585 & 0 \\ 0 & 0 & 1 \end{bmatrix}$	(0.2207, 0.1815)	$s\begin{bmatrix} 2.188\mathbf{e}^{6} & 0 & 2047.5 \\ 0 & 2.119\mathbf{e}^{6} & 1079.5 \\ 0 & 0 & 1 \end{bmatrix}$	(0.1757, 0.1202)
$\alpha = 15\,° \beta = 0°$	$\begin{bmatrix} -76.7193 & 0 & 0 \\ 0 & -79.6226 & 0 \\ 0 & 0 & 1 \end{bmatrix}$	(0.3919, 0.2723)	$s\begin{bmatrix} 1.185\mathbf{e}^{6} & 0 & 2047.5 \\ 0 & 1.477\mathbf{e}^{6} & 1079.5 \\ 0 & 0 & 1 \end{bmatrix}$	(0.1656, 0.1437)
$\alpha = 20\,° \beta = 0°$	$\begin{bmatrix} -76.7260 & 0 & 0 \\ 0 & -80.8303 & 0 \\ 0 & 0 & 1 \end{bmatrix}$	(0.4174, 0.1783)	$s\begin{bmatrix} 1.884\mathbf{e}^{6} & 0 & 2047.5 \\ 0 & 2.276\mathbf{e}^{6} & 1079.5 \\ 0 & 0 & 1 \end{bmatrix}$	(0.1747, 0.1188)

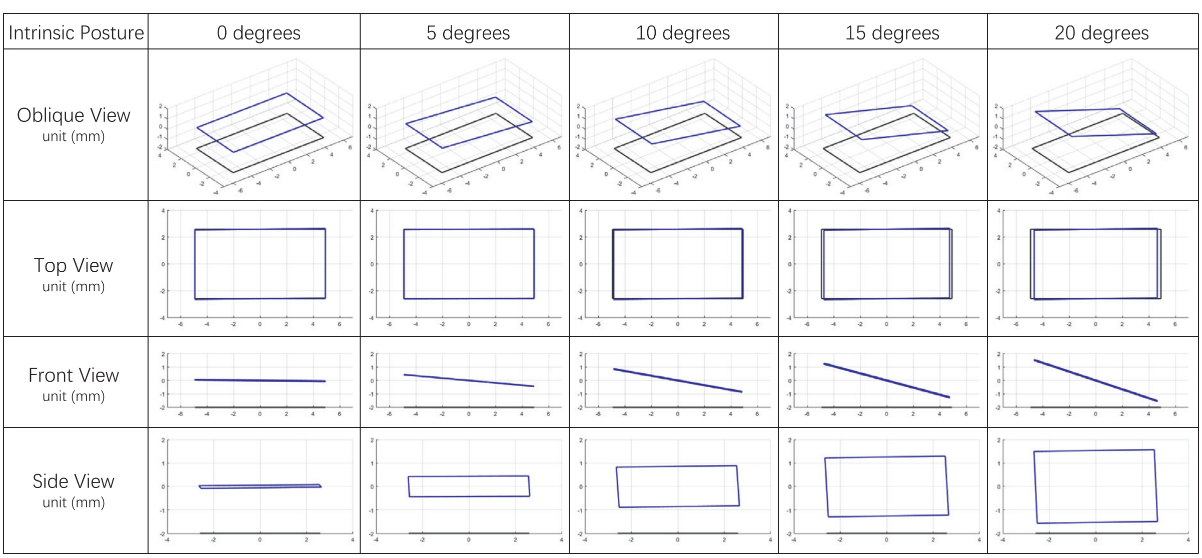

Fig. 11. The oblique, top, front, and side view of the retrieved posture of the tilt sensor planes in five cases.

In summary, all the parameters of the lens are calibrated perfectly with totally acceptable errors. The detailed calibration results are provided as in Fig. 12. In addition to the distribution map of the re-projection errors, the standard deviation of the re-projection errors in two axes are also provided in both pixel coordinates $(\boldsymbol{u}, \boldsymbol{v})$ and equivalent camera space coordinates $(\boldsymbol{x_C}, \boldsymbol{y_C})$, respectively.

5.2. *Stereo rectification of dual-Scheimpflug telecentric cameras*

5.2.1. *Experimental setup and stereo calibration result*

The stereo calibration and rectification of a dual-Scheimpflug telecentric system are performed to verify the proposed method introduced in Section 0. The experimental setup is as shown in Fig. 14. Two cameras are marked as $\boldsymbol{Left\ Camera}$ and $\boldsymbol{Right\ Camera}$, respectively. Each

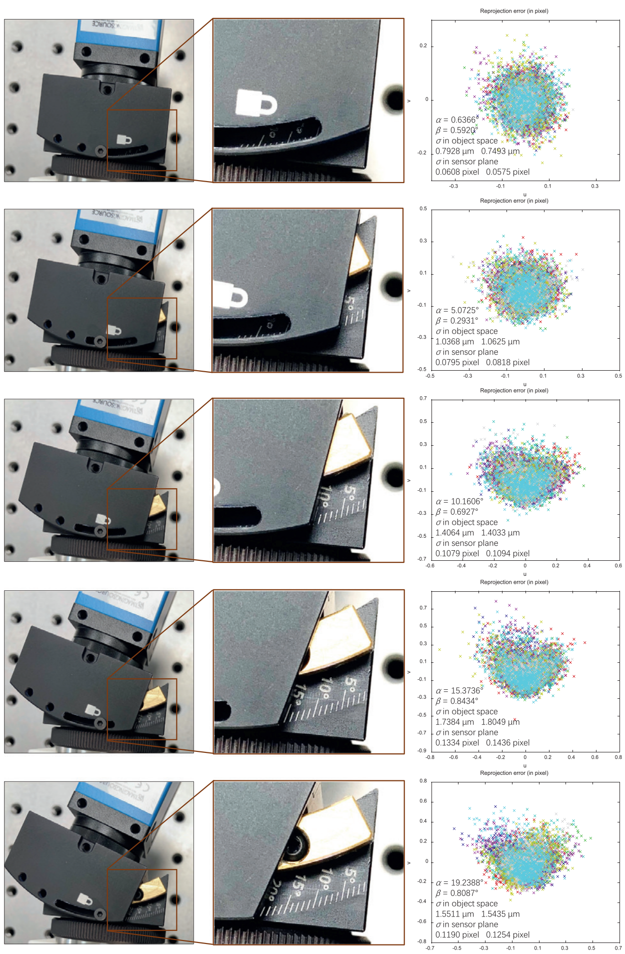

Fig. 12. The tilt angle of the Scheimpflug adaptor and the re-projection error of each situation.

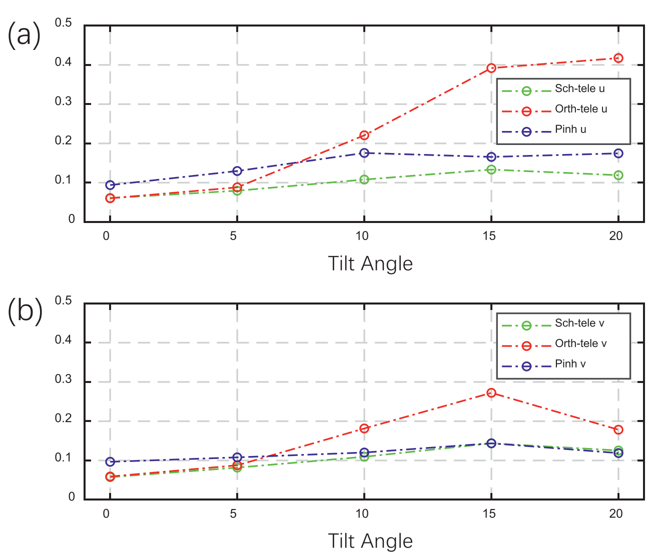

Fig. 13. The reprojection errors in $\boldsymbol{u}$ direction (a) and $\boldsymbol{v}$ direction (b) calculated using three models under five tilt angles.

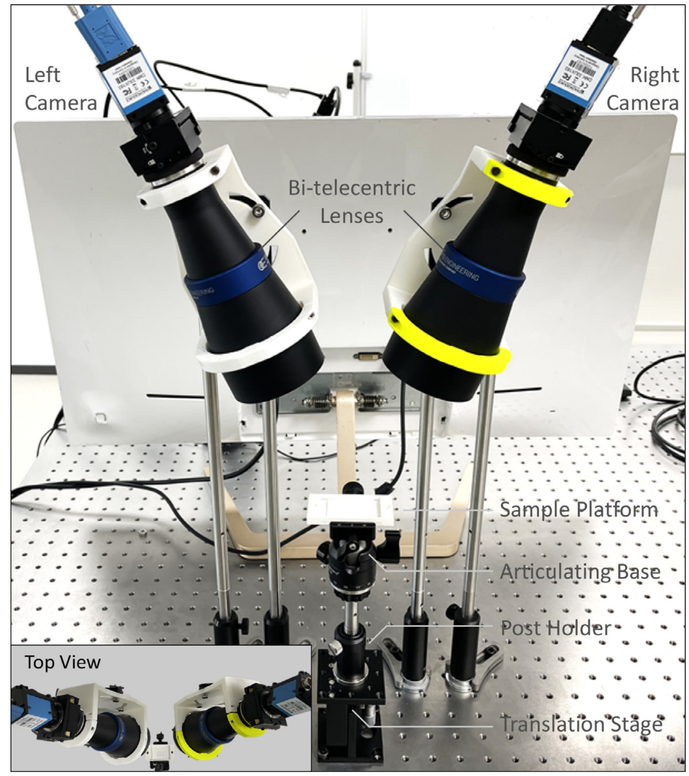

Fig. 14. Experomemtal setup of the stereo Scheimpflug telecentric lenses.

camera is equipped with a bi-telecentric lens, adjusted in Scheimpflug condition by tilt the Scheimpflug adaptor. A C-mount phase ring on the top side of the Scheimpflug adaptor is used to adjust the relative angle to the camera's thread interface. In regular applications, the ring is to avoid slanting images. However, in this subsection, we deliberately rotate the phase ring of the two cameras to five different angles in order to testify the effectiveness of the proposed stereo calibration and rectification methods.

The cameras need to be calibrated under the same world coordinate so that both cameras must share one calibration posture, and this posture determines the unique world coordinate for the stereo system. Without loss of generality, we take the horizontally placed posture to provide uniqueness. The posture ambiguity is eliminated by capturing another image after a preset displacement is applied on the calibration board.

Both lenses are placed on the top of the sample platform at an oblique angle, and we adjust the tilt angle of the Scheimpflug adaptor to focus the image plane on the sensor plane. Refer to Fig. 3, suppose the object plane is at the front focal plane of the first lens, a deviation of $\boldsymbol{\Delta l}$ occurs in the object space causes a deviation of $\boldsymbol{\Delta l'}$ in the image space. Denote $\boldsymbol{T_{mag}}$ and $\boldsymbol{A_{mag}}$ as the transverse magnification and axial magnification, respectively, and then we have

$$\boldsymbol{A_{mag}} = \boldsymbol{T_{mag}}^2 \approx \tan\boldsymbol{\theta}'/\tan\boldsymbol{\theta} \tag{40}$$

The transverse magnification of the lens is 0.185, therefore $\tan\boldsymbol{\theta}'/\tan\boldsymbol{\theta} \approx 0.185$ can be used as a criterion to guide the tilt angle setting. There is an $\sim 45^\circ$ angle between the optical axes of the left and right lenses in the experiment setup. According to Eq. (40), the tilt angles of the cameras are set $\sim \pm 3.3^\circ$.

The phase rings of the two cameras are rotated to five situations, as shown in Table 3. However, the angles (phases) are manually adjusted; therefore, the actually turned angels are not precisely the same as the preset values in Table 3. By applying the stereo calibration procedure introduced above, we calculated the cameras' intrinsic and extrinsic parameters under five situations.

Table 3
The calibrated camera parameters of the five camera pairs.

Rotated Phase(deg)	0 degrees		±5 degrees		±10 degrees		±15 degrees		±20 degrees	
Camera	L	R	L	R	L	R	L	R	L	R
Intrinsic Tilt Angles (deg)	$\alpha = 0.2858$ $\beta = -3.2740$	$\alpha = 0.4391$ $\beta = 3.4954$	$\alpha = 0.3640$ $\beta = -3.3642$	$\alpha = 0.3248$ $\beta = 3.8647$	$\alpha = 0.7895$ $\beta = -3.1917$	$\alpha = 0.6964$ $\beta = 3.7124$	$\alpha = 1.2733$ $\beta = -3.3280$	$\alpha = 0.7805$ $\beta = 3.5894$	$\alpha = 1.2542$ $\beta = -2.9789$	$\alpha = 0.6611$ $\beta = 3.2119$
Extrinsic Rotation Angle(deg)	22.4091	22.0505	22.5902	22.1257	23.0527	21.5341	21.7055	22.4668	22.7571	20.3988
Extrinsic Rotation Axis (normalized)	$\begin{bmatrix}-0.5836\\1.1547\\-0.5710\end{bmatrix}$	$\begin{bmatrix}0.5950\\-1.1545\\0.5595\end{bmatrix}$	$\begin{bmatrix}-0.5767\\1.1547\\-0.5780\end{bmatrix}$	$\begin{bmatrix}0.5175\\-1.1527\\0.6352\end{bmatrix}$	$\begin{bmatrix}-0.6272\\1.1532\\-0.5260\end{bmatrix}$	$\begin{bmatrix}0.4718\\-1.1486\\0.6768\end{bmatrix}$	$\begin{bmatrix}-0.6841\\1.1477\\-0.4635\end{bmatrix}$	$\begin{bmatrix}0.4380\\-1.1443\\0.7063\end{bmatrix}$	$\begin{bmatrix}-0.7611\\1.1326\\-0.3714\end{bmatrix}$	$\begin{bmatrix}0.4784\\-1.1493\\0.6710\end{bmatrix}$

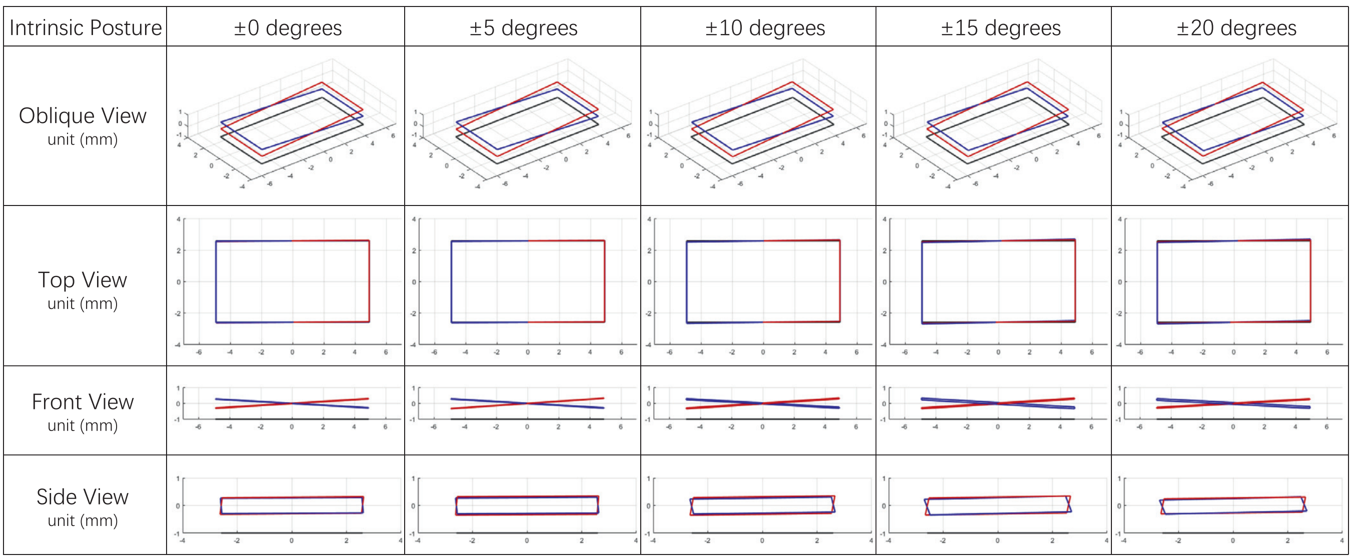

Fig. 15. Camera sensor postures retrieved in five situations.

Based on the retrieved $\mathbf{A_m}$, we can derive $\boldsymbol{j}$, $\boldsymbol{k}$, and $\boldsymbol{l}$ by Eq. (22). Then the sensor tilt angle $\boldsymbol{\alpha}$ and $\boldsymbol{\beta}$ can also be obtained by solving Eq. (24), which are listed in the second row in Table 3. A positive s_4 corresponds to a negative $\boldsymbol{l}$ and a clockwise rotation of the sensor around the optical axis $\boldsymbol{Z_C}$. By using $Rodrigues'\ rotation\ formula$ the rotation matrix is converted to an angle and an axis represented by a vector about which the target rotates the angle. The rotation matrixes of left and right cameras under each situation make two camera coordinate systems rotate nearly the same angles but in opposite directions relative to the common plane where the world coordinate system locates. It should be noted that the common plane is not perfectly horizontal, together with the sensor tilt, makes the rotation matrix of the camera pair not be strictly symmetrical, which is consistent with and can be confirmed from the data in Table 3.

The spatial location of sensor plane $\boldsymbol{\Pi}$ relative to the ideal image plane $\boldsymbol{\Pi}p$ is shown in Fig. 15. The blue rectangle represents the left camera's sensor tilt, while the red rectangle represents the right camera's sensor tilt. The black rectangle is a horizontally placed sensor plane for reference. From the result, we can see that the sensor orientation varies a little bit, only around $\boldsymbol{X_C}$ and $\boldsymbol{Y_C}$ axis but not $\boldsymbol{Z_C}$. This is because the lens is symmetrical about the optical axis so that the rotation around $\boldsymbol{Z_C}$ axis does not make any sense to the imaging. The effect of the rotation around $\boldsymbol{Z_C}$ axis will not change the intrinsic parameters but the extrinsic parameters. From the side view, we can see that when the angle of the phase ring is zero, the sensor only tilts around its $\mathbf{u}$ axis. But when the angle of the phase ring gradually increases, the sensor gradually appears significant tilt around its $\mathbf{v}$ axis.

Fig. 16 shows the extrinsic parameters in the form of spatial graphs. The black rectangle represents the calibration board, which is also the $\boldsymbol{O-XY}$ plane of the world coordinate system. The blue rectangle and the red rectangle respectively represent the $\boldsymbol{O_C}$-$\boldsymbol{X_C Y_C}$ plane of the left and right camera. The telecentricity renders the camera coordinates insensitive in the change along its $\boldsymbol{Z_C}$ axis. Therefore for ease of display, the camera coordinate systems are shifted along their $\boldsymbol{Z_C}$ axes to make them be closer for observation. In the meanwhile, the world coordinate system is also shifted along its $\boldsymbol{Z}$ axis.

5.2.2. Stereo rectification result

The stereo rectification can be realized based on Eq. (39). For each integral pixel coordinate $\boldsymbol{p'_L}$ of the rectified image, its corresponding sub-pixel coordinate on the original image is obtained by calculating $\boldsymbol{p_L}$. The rectified image can be reconstructed by sub-pixel interpolating the original image based on $\boldsymbol{p_L}$. In the first experiment, the calibration board image representing the shared world coordinate system, is used as the original image pair. The rectification result is presented in Fig. 17, from which we can clearly figure out that after the rectification, the pixels in the left and right rectified images are strictly transformed in the same vertical position.

In order to verify the effectiveness of the proposed method for arbitrarily placed objects, a QR code pattern is printed and used as the target. The rectified result is as shown in Fig. 18, in which the left two columns are the initially captured image pairs and the right two columns are the rectified images. The cameras are rotated to the same relative angles as that set in the last experiment. As shown in the top view in Fig. 16, as the extrinsic rotation angles increases, the captured targets correspondingly rotate to opposite angles from zero degrees to about twenty degrees. Differently, the QR code patterns in the rectified im-

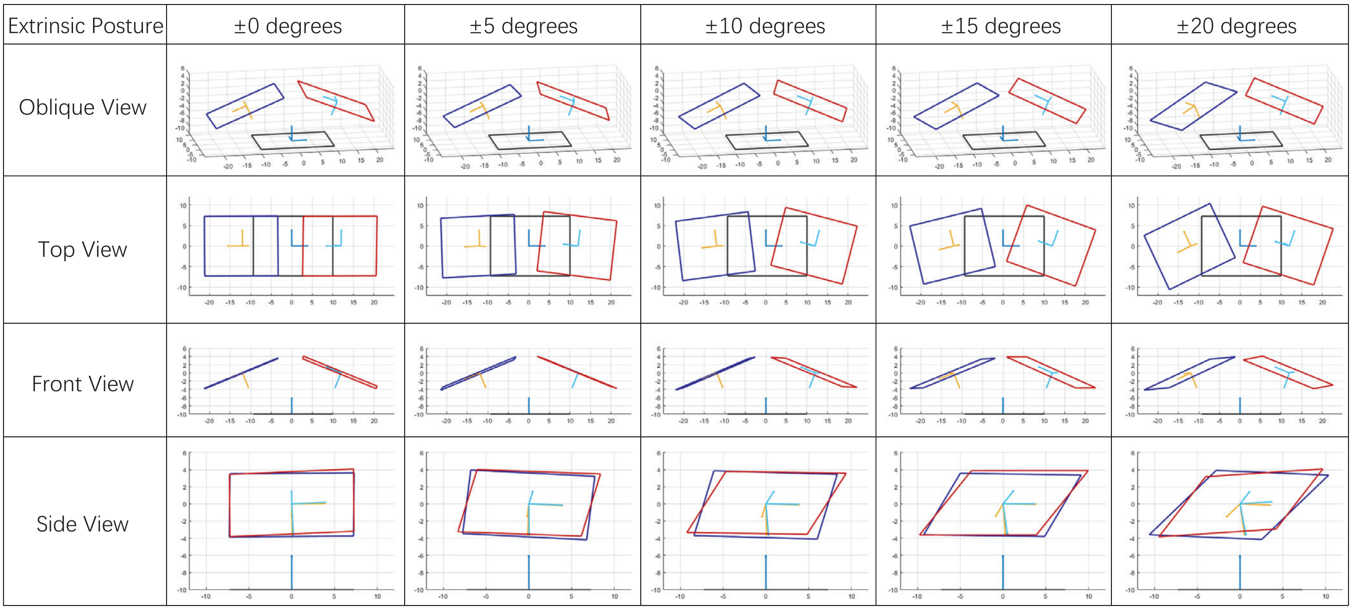

Fig. 16. The spatial perspective of extrinsic rotation in five situations.

ages look rotated back to a consistent shape through the rectification, and the epipolar lines are adjusted to the same horizontal position.

6. Discussion

6.1. The effect of the extrinsic ambiguity on the measurement

As we know that the world coordinates of the stereo vision system are determined by the spatial position of one calibration pattern, and the relative position of the camera depends on the calculated extrinsic parameters. In order to make the disparity fully reflected on the cameras, the angle and baseline of the cameras need to be carefully tackled in triangulation. However, if the retrieved extrinsic parameters are not accurate, the camera's position in the actual space cannot be truly reconstructed. As shown in Fig. 8, when the external parameters are ambiguous, the two cameras' spatial positions may appear very close. In this way, both the angle and baseline between the two cameras will become much smaller, far from the structure requirements of binocular measurements.

With the change of the signs of $\boldsymbol{r}_{13}$ and $\boldsymbol{r}_{23}$ in Eq. (24), there will be a total of 16 different initial combinations of rotation matrix values before optimization. In order to explain the measurement error introduced by the ambiguity of the rotation matrix, we calibrated the system with ten calibration images and deliberately changed the signs of $\boldsymbol{r}_{13}$ and $\boldsymbol{r}_{23}$ and use the new $\boldsymbol{r}_{13}$ and $\boldsymbol{r}_{23}$ as the initial values to re-optimize the camera parameters. The left and right cameras both have four posture candidates, resulting in sixteen possible posture combinations, as shown in Fig. 19.

In fact, for two bi-telecentric cameras with two optical axes intersecting or close to each other, the ambiguity of the rotation angle around $\boldsymbol{X}$ axis will be clearly reflected in the structure shown in Fig. 19. Meanwhile, the ambiguity of the rotation angle around $\boldsymbol{Y}$ axis is too subtle to distinguish, so it is not easy to judge whether the rotation angle is correct through direct observation.

As shown in Fig. 20, the reconstruction of the calibration pattern is performed here to show the influence of the external parameter's ambiguity on the measurement. The 3D data of the calibration markers reconstructed from the wrong posture combination appears stretched to several directions and mirrored. Even subtle differences can cause significant distortion to the 3D data, which is not allowed in high-precision vision-based measures. Nevertheless, the good news is that the rotation angle around $\boldsymbol{Y}$ axis can also be retrieved through a converged iteration procedure even with an incorrect initial value if specific conditions are satisfied, which will be discussed in the next sub-section.

6.1.1. The effect of the calibration posture on the intrinsic matrix

The number and position of the calibration postures decide whether the solution exists and the camera parameters' accuracy. Since four unknowns exist in Eq. (20), at least four calibration patterns are required. The rotation and translation matrix need to be controlled to ensure that the equations in Eq. (20) are linearly independent of each other. To be specific, the augmented matrix composed of equation Eq. (19) derived from all the calibration patterns should be full rank, and if not, the solution would be quite unstable or does not exist. Each calibration posture corresponds to an equation, and three situations will cause the augmented matrix to be rank deficient.

Situation 1 Only translation between the calibration postures

In this situation, referring to Eq. (13), only $\boldsymbol{t}_x$ and $\boldsymbol{t}_y$ changes, followed by the changing of $\boldsymbol{h}_{14}$, and $\boldsymbol{h}_{24}$ while $\boldsymbol{h}_{11}$, $\boldsymbol{h}_{12}$, $\boldsymbol{h}_{21}$, and $\boldsymbol{h}_{22}$ remain unchanged. Therefore, no contribution is made by translation to the augmented matrix.

Situation 2 Only rotation around the $\boldsymbol{Z}$-axis

Suppose that the world coordinate system of a particular calibrated posture is obtained by successively rotating the camera coordinate system around its $\boldsymbol{Z}_C$-axis, $\boldsymbol{Y}_C$-axis, and $\boldsymbol{X}_C$-axis by θ_3, θ_2, θ_1, respectively. The corresponding rotation matrix is

$$\begin{bmatrix} \cos(\theta_2)\cos(\theta_3) & -\cos(\theta_2)\sin(\theta_3) & \sin(\theta_2) \\ \cos(\theta_1)\sin(\theta_3) - \cos(\theta_3)\sin(\theta_1)\sin(\theta_2) & \cos(\theta_1)\cos(\theta_3) - \sin(\theta_1)\sin(\theta_2)\sin(\theta_3) & -\cos(\theta_2)\sin(\theta_1) \\ \sin(\theta_1)\sin(\theta_3) - \cos(\theta_1)\cos(\theta_3)\sin(\theta_2) & \cos(\theta_3)\sin(\theta_1) + \cos(\theta_1)\sin(\theta_2)\sin(\theta_3) & \cos(\theta_1)\cos(\theta_2) \end{bmatrix} \quad (41)$$

This matrix is also the rotation matrix $\mathbf{R}$ from the coordinates of the points in the world coordinate system to the camera coordinates system. By incorporating Eq. (41) into the homography matrix, we can simplify

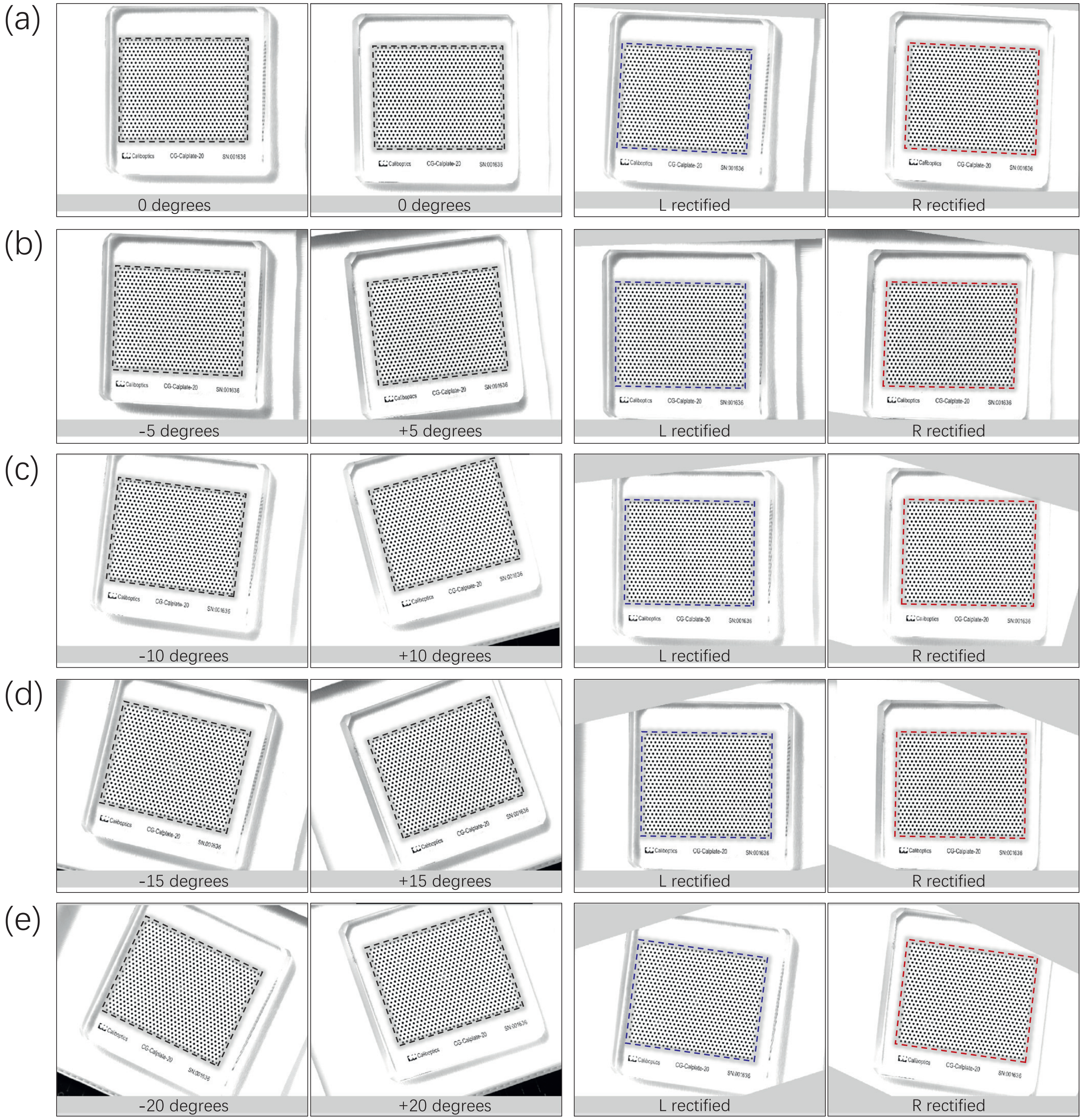

Fig. 17. The rectification of the images containing the calibration pattern. (a) – (e) Orignal and rectified image pairs under five rotation angles. Black rectangles mark the circled areas on the original image pairs. Blue and red rectangles respectively mark the circled areas on the rectified images.

the coefficients in Eq. (20) as

$$\begin{bmatrix} 1 \\ -\left(h_{11}^2+h_{12}^2\right) \\ -\left(h_{21}^2+h_{22}^2\right) \\ 2\left(h_{11}h_{21}+h_{12}h_{22}\right) \\ -\left(h_{12}h_{21}-h_{11}h_{22}\right)^2 \end{bmatrix} \begin{bmatrix} 1 \\ -j^2\cos^2\theta_2 \\ -k^2\cos^2\theta_1-\sin^2\theta_1\sin^2\theta_2-2l\sin\theta_1\sin\theta_2\cos\theta_2-l^2\cos^2\theta_2 \\ 2j\left(l\cos^2\theta_2+\sin\theta_1\sin\theta_2\cos\theta_2\right) \\ -j^2k^2\cos^2\theta_1\cos^2\theta_2 \end{bmatrix} \tag{42}$$

If another calibration posture has the same $\boldsymbol{Z}$-axis direction, the third column in Eq. (41) is the same as the first one. Then the angles of the two postures around the $\boldsymbol{X}_C$-axis, $\boldsymbol{Y}_C$-axis are the same, being both θ_1 and θ_2. This means that the two calibration postures will provide the same augmentation coefficient as Eq. (42) states, which means the calibration image formed by the rotation in the calibration plane (around the $\boldsymbol{Z}$-axis) has no contribution to the solution of the equation.

Fig. 18. The rectification of the images containing the QR code pattern. (a) – (e) Orignal and rectified image pairs under five rotation angles. The correct information can be scanned by a smartphone from both the original images and the rectified images.

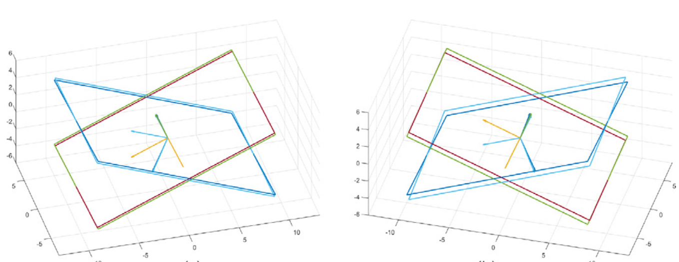

Fig. 19. Four initial candidates of the rotation matrix of the left camera (a) and right camera (b).

Situation 3 Different posture but the same picture captured

This is a situation that is easy to explain and understand but unlikely to happen. One calibration image corresponds to two spatial postures of the board, with their depth distribution being mirrored along the Z-axis. In this case, the rotation angles around three axes should all be the same but in the opposite direction, which has a reasonably small probability of occurrence.

The above-introduced situations should be consciously avoided to make all the calibration images provide valid equations to Eq. (20). Besides, to ensure that the augmented matrix has a smaller condition number to obtain a more stable solution, it is necessary to avoid the rotation

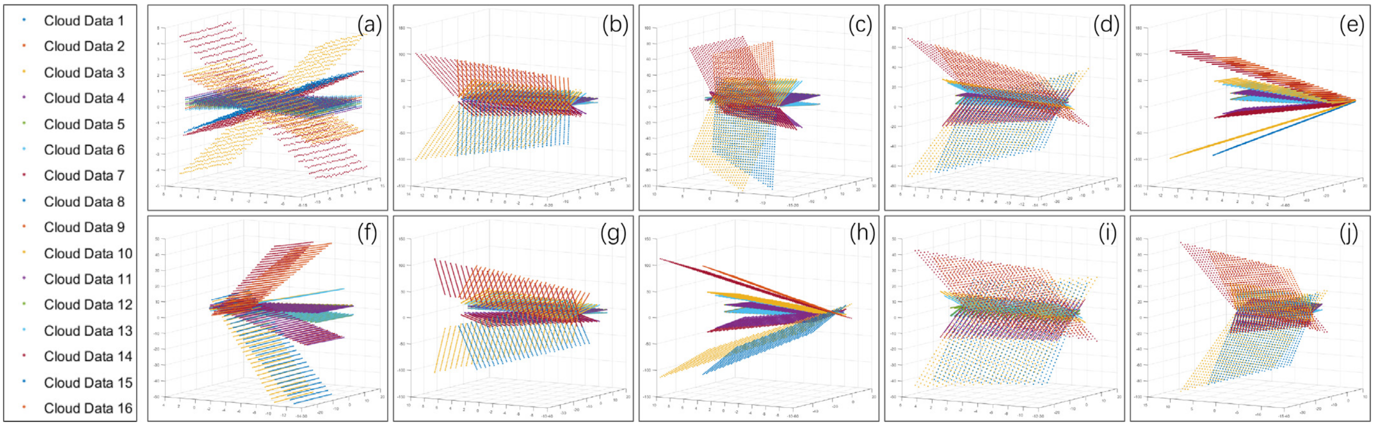

Fig. 20. The reconstructed cloud data of the markers from ten calibration patterns. Each subgraph corresponds to one calibration image and has sixteen results caused by the 4 × 4 combinations.

angle θ_1 and θ_2 from becoming zero degrees or ninety degrees (actually impossible).

7. Conclusions

In this paper, we derived a concise imaging model and proposed a plane calibration method to solve the camera parameters in the calibration of telecentric lenses in Scheimpflug conditions. The intrinsic parameters containing the sensor tilt angles and the lens magnification are expressed as three parameters that can be directly solved base on the homography matrix. On this basis, the Scheimpflug stereo rectification method was proposed and verified through two sets of experiments.

In the discussion part, we have the conclusion that the initial rotation angles need not be precisely the ground truth. The ambiguity can be eliminated through $Rodrigues'\ rotation\ formula$ based optimization procedure provided that the rotation direction is roughly correct. We also discussed how the postures of the calibration boards influence the calibration accuracy and concluded several situations under which the postures are ineffective.

The success of the calibration and rectification of the telecentric lens in Scheimpflug conditions will offer a valuable reference in system design with a more considerable measurement depth of field for fast and accurate microscopic 3D measurement applications such as DIC, structured light projection.

Declaration of Competing Interest

We declare that we have no financial and personal relationships with other people or organizations that can inappropriately influence our work, there is no professional or other personal interest of any nature or kind in any product, service and/or company that could be construed as influencing the position presented in, or the review of, the manuscript entitled.

CRediT authorship contribution statement

Yan Hu: Conceptualization, Methodology, Writing – original draft, Data curation. **Zhongwei Liang:** Software, Validation, Visualization. **Shijie Feng:** Resources. **Wei Yin:** Validation. **Jiaming Qian:** Investigation. **Qian Chen:** Funding acquisition. **Chao Zuo:** Writing – review & editing, Supervision.

Acknowledgments

This work was supported by National Natural Science Foundation of China (62005121, 61722506, 61705105), China Postdoctoral Science Foundation (2019M661843), National Key R&D Program of China (2017YFF0106403), Leading Technology of Jiangsu Basic Research Plan (BK20192003), National Defense Science and Technology Foundation of China (2019-JCJQ-JJ-381), “333 Engineering” Research Project of Jiangsu Province (BRA2016407), Jiangsu Provincial “One belt and one road” innovation cooperation project (BZ2020007), Fundamental Research Funds for the Central Universities (30920032101, 30919011222), and Open Research Fund of Jiangsu Key Laboratory of Spectral Imaging & Intelligent Sense (3091801410411).

References

[1] Hu Y, Chen Q, Feng S, Zuo C. Microscopic fringe projection profilometry: a review. Opt Lasers Eng 2020:106192. doi:10.1016/j.optlaseng.2020.106192.
[2] Zhang S. Recent progresses on real-time 3D shape measurement using digital fringe projection techniques. Opt Lasers Eng 2010;48:149–58. doi:10.1016/j.optlaseng.2009.03.008.
[3] Hu Y, Chen Q, Feng S, Tao T, Asundi A, Zuo C. A new microscopic telecentric stereo vision system – calibration, rectification, and three-dimensional reconstruction. Opt Lasers Eng 2019;113:14–22. doi:10.1016/j.optlaseng.2018.09.011.
[4] Zhang S, Li B, Ren F, Dong R. High-precision measurement of binocular telecentric vision system with novel calibration and matching methods. IEEE Access 2019;7:54682–92. doi:10.1109/ACCESS.2019.2913181.
[5] Nalpantidis L, Sirakoulis GC, Gasteratos A. Review of stereo matching algorithms for 3D vision. DIVA 2007.
[6] Dhond UR, Aggarwal JK. Structure from stereo-a review. IEEE Trans Syst Man Cybern 1989;19:1489–510. doi:10.1109/21.44067.
[7] Chen Z, Liao H, Zhang X. Telecentric stereo micro-vision system: calibration method and experiments. Opt Lasers Eng 2014;57:82–92. doi:10.1016/j.optlaseng.2014.01.021.
[8] Hu Y, Chen Q, Tao T, Li H, Zuo C. Absolute three-dimensional micro surface profile measurement based on a Greenough-type stereomicroscope. Meas Sci Technol 2017;28:045004. doi:10.1088/1361-6501/aa5a2d.
[9] Hu Y, Chen Q, Zhang Y, Feng S, Tao T, Li H, et al. Dynamic microscopic 3D shape measurement based on marker-embedded Fourier transform profilometry. Appl Opt 2018;57:772. doi:10.1364/AO.57.000772.
[10] Hu Y, Chen Q, Feng S, Tao T, Li H, Zuo C. Real-time microscopic 3D shape measurement based on optimized pulse-width-modulation binary fringe projection. Meas Sci Technol 2017;28:075010. doi:10.1088/1361-6501/aa7277.
[11] Li D, Tian J. An accurate calibration method for a camera with telecentric lenses. Opt Lasers Eng 2013;51:538–41. doi:10.1016/j.optlaseng.2012.12.008.
[12] Huiyang L, Zhong C, Xianmin Z. Calibration of camera with small FOV and DOF telecentric lens. IEEE 2013:498–503. doi:10.1109/ROBIO.2013.6739509.
[13] Yao L, Liu H. A flexible calibration approach for cameras with double-sided telecentric lenses. Int J Adv Robot Syst 2016;13:82. doi:10.5772/63825.
[14] Guan B, Yao L, Liu H, Shang Y. An accurate calibration method for non-overlapping cameras with double-sided telecentric lenses. Opt – Int J Light Electron Opt 2017;131:724–32. doi:10.1016/j.ijleo.2016.11.156.
[15] Peng J, Wang M, Deng D, Liu X, Yin Y, Peng X. Distortion correction for microscopic fringe projection system with Scheimpflug telecentric lens. Appl Opt 2015;54:10055. doi:10.1364/AO.54.010055.
[16] Liu H, Lin H, Yao L. Calibration method for projector-camera-based telecentric fringe projection profilometry system. Opt Express 2017;25:31492–508. doi:10.1364/OE.25.031492.
[17] Huang PS. Novel method for structured light system calibration. Opt Eng 2006;45:083601. doi:10.1117/1.2336196.

[18] Huang L, Chua PSK, Asundi A. Least-squares calibration method for fringe projection profilometry considering camera lens distortion. Appl Opt 2010;49:1539. doi:10.1364/AO.49.001539.
[19] Li B, Zhang S. Flexible calibration method for microscopic structured light system using telecentric lens. Opt Express 2015;23:25795. doi:10.1364/OE.23.025795.
[20] Liu H, Su W-H, Reichard K, Yin S. Calibration-based phase-shifting projected fringe profilometry for accurate absolute 3D surface profile measurement. Opt Commun 2003;216:65–80. doi:10.1016/S0030-4018(02)02290-3.
[21] Rao L, Da F, Kong W, Huang H. Flexible calibration method for telecentric fringe projection profilometry systems. Opt Express 2016;24:1222–37. doi:10.1364/OE.24.001222.
[22] Zhang Z. A flexible new technique for camera calibration. IEEE Trans Pattern Anal Mach Intell 2000;22:1330–4. doi:10.1109/34.888718.
[23] Tanaka H, Sumi Y, Matsumoto Y. A solution to pose ambiguity of visual markers using Moiré patterns. IEEE 2014:3129–34. doi:10.1109/IROS.2014.6942995.
[24] Beermann R, Quentin L, Kästner M, Reithmeier E. Calibration routine for a telecentric stereo vision system considering affine mirror ambiguity. Opt Eng 2020;59::1. doi:10.1117/1.OE.59.5.054104.
[25] Legarda A, Izaguirre A, Arana N, Iturrospe A. A new method for Scheimpflug camera calibration. 2011 10th. Int. Workshop Electron. Control Meas. Signals 2011:1–5. doi:10.1109/IWECMS.2011.5952376.
[26] Hamrouni S, Louhichi H, Aissia HB, Elhajem M. A new method for stereo- cameras self-calibration in Scheimpflug condition 2012:10.
[27] Cornic P, Illoul C, Cheminet A, Le Besnerais G, Champagnat F, Le Sant Y, et al. Another look at volume self-calibration: calibration and self-calibration within a pinhole model of Scheimpflug cameras. Meas Sci Technol 2016;27:094004. doi:10.1088/0957-0233/27/9/094004.
[28] Sun C, Liu H, Jia M, Chen S. Review of calibration methods for Scheimpflug camera. J Sens 2018;2018:1–15. doi:10.1155/2018/3901431.
[29] Louhichi H, Fournel T, Lavest JM, Aissia HB. Self-calibration of Scheimpflug cameras: an easy protocol. Meas Sci Technol 2007;18:2616–22. doi:10.1088/0957-0233/18/8/037.
[30] Mei Q, Gao J, Lin H, Chen Y, Yunbo H, Wang W, et al. Structure light telecentric stereoscopic vision 3D measurement system based on Scheimpflug condition. Opt Lasers Eng 2016;86:83–91. doi:10.1016/j.optlaseng.2016.05.021.
[31] Wang M, Yin Y, Deng D, Meng X, Liu X, Peng X. Improved performance of multi-view fringe projection 3D microscopy. Opt Express 2017;25:19408. doi:10.1364/OE.25.019408.
[32] Steger C. A Comprehensive and Versatile Camera Model for Cameras with Tilt Lenses. Int J Comput Vis 2017;123:121–59. doi:10.1007/s11263-016-0964-8.
[33] Yin Y, Wang M, Gao BZ, Liu X, Peng X. Fringe projection 3D microscopy with the general imaging model. Opt Express 2015;23:6846. doi:10.1364/OE.23.006846.
[34] Pan B, Qian K, Xie H, Asundi A. Two-dimensional digital image correlation for in-plane displacement and strain measurement: a review. Meas Sci Technol 2009;20:062001. doi:10.1088/0957-0233/20/6/062001.
[35] Zuo C, Huang L, Zhang M, Chen Q, Asundi A. Temporal phase unwrapping algorithms for fringe projection profilometry: a comparative review. Opt Lasers Eng 2016;85:84–103. doi:10.1016/j.optlaseng.2016.04.022.
[36] Zuo C, Feng S, Huang L, Tao T, Yin W, Chen Q. Phase shifting algorithms for fringe projection profilometry: a review. Opt Lasers Eng 2018;109:23–59. doi:10.1016/j.optlaseng.2018.04.019.
[37] Feng S, Chen Q, Gu G, Tao T, Zhang L, Hu Y, et al. Fringe pattern analysis using deep learning. Adv Photon 2019;1(1). doi:10.1117/1.AP.1.2.025001.
[38] Hu Y, Feng S, Tao T, Zuo C, Chen Q, Asundi A. Calibration of telecentric cameras with distortion center estimation. Sixth int. conf. opt. photonic eng. IcOPEN, 10827; 2018. International Society for Optics and Photonics; 2018.
[39] Zuo C, Chen Q, Gu G, Feng S, Feng F. High-speed three-dimensional profilometry for multiple objects with complex shapes. Opt Express 2012;20:19493. doi:10.1364/OE.20.019493.
[40] Qian J, Feng S, Tao T, Hu Y, Liu K, Wu S, et al. High-resolution real-time 360° 3D model reconstruction of a handheld object with fringe projection profilometry. Opt Lett 2019;44:5751. doi:10.1364/OL.44.005751.
[41] Liu H, Zhu Z, Yao L, Dong J, Chen S, Zhang X, et al. Epipolar rectification method for a stereovision system with telecentric cameras. Opt Lasers Eng 2016;83:99–105. doi:10.1016/j.optlaseng.2016.03.008.
[42] Fusiello A, Trucco E, Verri A. A compact algorithm for rectification of stereo pairs. Mach Vis Appl 2000;12:16–22. doi:10.1007/s001380050120.
[43] Abraham S, Förstner W. Fish-eye-stereo calibration and epipolar rectification. ISPRS J Photogramm Remote Sens 2005;59:278–88. doi:10.1016/j.isprsjprs.2005.03.001.